Measurement of exclusive π^+-argon interactions using ProtoDUNE-SP

S. Abbaslu *et al.*[*]
(DUNE Collaboration)

(Received 19 November 2025; accepted 26 March 2026; published 3 June 2026)

We present the measurement of π^+-argon inelastic cross sections using the ProtoDUNE single-phase liquid argon time projection chamber in the incident π^+ kinetic energy range of 500–800 MeV in multiple exclusive channels (absorption, charge exchange, and the remaining inelastic interactions). The results of this analysis are important inputs to simulations of liquid argon neutrino experiments such as the Deep Underground Neutrino Experiment and the Short Baseline Neutrino program at Fermi National Accelerator Laboratory. They will be employed to improve the modeling of final state interactions within neutrino event generators used by these experiments, as well as the modeling of π^+-argon secondary interactions within the liquid argon. This is the first measurement of π^+-argon absorption at this kinetic energy range as well as the first ever measurement of π^+-argon charge exchange.

DOI: 10.1103/nm5s-4cnw

I. INTRODUCTION

Liquid argon time projection chamber (LArTPC) neutrino experiments, such as the Short Baseline Neutrino program at Fermi National Accelerator Laboratory and—in the future—the Deep Underground Neutrino Experiment (DUNE) [1], precisely measure energy-dependent neutrino oscillations by observing the charged particles emitted when neutrinos interact with the argon in the detectors. They attempt to identify the flavor of the neutrinos by tagging the charged lepton produced from charged-current interactions and to reconstruct the neutrino energy from all of the observed particles. Key challenges lie in understanding how energy is shared among the emitted particles and how much energy is lost to unobserved neutral or low-energy particles. Final state interactions (FSI)—of particles within the nucleus immediately following a neutrino interaction—have a large impact on energy smearing, as energy can be transferred to undetected particles. Additionally, these interactions, along with interactions with the argon of the particles escaping the nucleus following the neutrino interaction [so-called "secondary interactions" (SI)], can impact the ability to correctly identify the flavor of the incident neutrino. Thus, the modeling uncertainties of FSI and SI limit the resolution and bias the extraction of oscillation parameters but can be constrained by dedicated hadron-nucleus scattering data [2,3]. For the DUNE oscillation program, understanding π-argon FSI and SI will be particularly important, as significant portions of $\overset{(-)}{\nu}_\mu$ charged-current events in its detectors will contain a $\pi^\pm$ in the final state—for example, resonant pion production accounts for roughly 40% of interactions at DUNE [4].

ProtoDUNE single-phase (ProtoDUNE-SP) serves as a test bed to test the technology of DUNE's horizontal-drift far detector module. It also acts as a source for hadron-argon scattering data from its charged particle test beam. In this work, we present the analysis of π^+-argon interactions with pion kinetic energy between 500 and 800 MeV. Several categories of interactions (depending on their final state signature) were targeted for study within this analysis:

(i) Absorption: no charged pions above 150 MeV/c momentum and no π^0.
(ii) Charge exchange: no charged pions above 150 MeV/c momentum and at least one π^0.
(iii) Other interactions[1]: at least one charged pion above 150 MeV/c momentum.

While the majority of pions will be produced with lower kinetic energy as a result of the ν-argon interactions seen at DUNE, the energy range covered by this analysis remains an important source of data with which to constrain the FSI models within neutrino event generators. The spread of these models, hinting at the uncertainty of the rates of these interactions—and thus the importance of this analysis—can be seen within the model comparisons within Ref. [2].

[*]Full author list given at the end of the article.

Published by the American Physical Society under the terms of the Creative Commons Attribution 4.0 International license. Further distribution of this work must maintain attribution to the author(s) and the published article's title, journal citation, and DOI. Funded by SCOAP[3].

[1]Note: this will contain contributions from π^+-to-π^+ scattering, double charge exchange (π^+-to-π^-), and pion production.

II. EXPERIMENTAL APPARATUS

ProtoDUNE-SP is a LArTPC housed in a cryostat located in the CERN North Area [5,6]. It collected data from the H4-VLE charged particle beam line in the fall of 2018 and cosmic-ray particles until its decommissioning in 2021. The beam instrumentation, described further in Sec. II B, provides event triggering for the ProtoDUNE-SP detector, as well as particle identification (PID). The analysis within this paper uses roughly 153 k π^+/μ^+ beam triggers from data taken during this time. Note that $\pi^\pm$ and $\mu^\pm$ are indistinguishable within the beam line PID.

A. ProtoDUNE-SP detector

The ProtoDUNE-SP LArTPC is separated into two drift volumes by a central, vertical cathode plane, with two sets of anode planes on either side of the cathode. Each of the two TPC volumes has dimensions of $3.6\,\mathrm{m}(x) \times 6.1\,\mathrm{m}(y) \times 7.0\,\mathrm{m}(z)$.[2] The cathode and anode planes are biased such that the nominal drift electric field magnitude is 500 V/cm. A field cage, which stabilizes the shape of the electric field at the lateral edges of the detector, covers the four nonanode faces of the detector. The beam enters into one drift volume by passing through the field cage near the cathode and points roughly 11° below horizontal and 10° toward the beam-side anode planes. To reduce energy loss upstream of the active TPC volume, a cylindrical "beam plug" is installed between the cryostat and the field cage. It is made of alternating fiberglass and stainless steel rings, capped at both ends with fiberglass plates. The plug is filled with nitrogen at 1.3 bar in order to balance against the pressure of the liquid argon while limiting the amount of material through which the test beam particles traverse. An illustration of the beam-side drift volume of ProtoDUNE-SP is shown in Fig. 1. As shown in this figure, we define a fiducial volume wherein we perform our measurement. With the origin of our coordinate system set to the bottom corner of the central cathode closest to where the beam enters the TPC, the fiducial volume boundaries are given by (−360 cm, 0 cm), (0 cm, 700 cm), and (30 cm, 215 cm), respectively, for x, y, and z.

The two sets of anode planes on either side of the cathode are each formed of three anode plane assemblies (APAs) oriented side by side. Each APA consists of four planes of wires, three of which are instrumented for readout. The outermost (relative to the center of the APA frame) plane is uninstrumented and provides shielding from long-range induction effects for the sense planes. The wires are biased such that ionization electrons drift past the shielding plane and two instrumented "induction" planes before depositing onto the final instrumented "collection" plane. The readout planes are oriented 35.7°, −35.7°, and 0° with respect to the vertical direction. Thus, combinations of signals on the three wire planes provide 2D positioning in the yz plane of the APA. The third dimension, x, correlates with the time the charge arrived on the wires. The APAs on the beam-side drift volume were installed with "electron diverters" in the gaps between pairs of APAs. These consist of a pair of electrode strips and were intended to prevent ionization from drifting into the region between APAs. However, an electrical short to ground prevented the use of these during operation and were left unpowered. The unpowered electron diverters absorbed ionization electrons created nearby in the z dimension, resulting in distortion to the tracks in the TPC and loss of charge available for reconstruction. As such, we limit their effect on this analysis (*vis-à-vis* selection performance and energy reconstruction) by separating out tracks which approach the affected region in z from our signal interaction candidates.

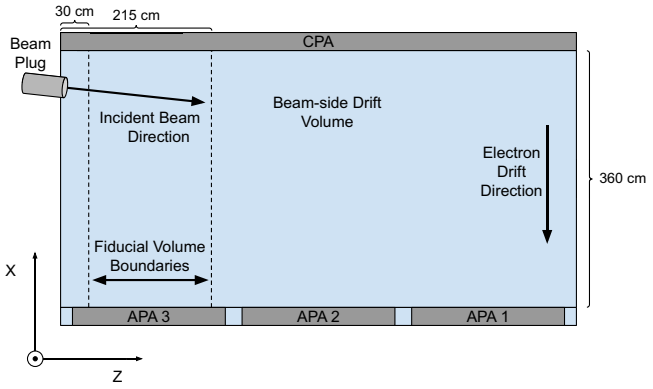

FIG. 1. Bird's-eye view of the beam-side drift volume of ProtoDUNE-SP (one-half of the full detector). The vertical, dotted line indicates the cut in the reconstructed z position used within the event selection. Along the top of the illustration is the cathode plane assembly (CPA) which separates the two drift volumes. Each beam-side anode plane assembly (APA) is shown at the bottom. Note that the non-beam-side drift volume is not shown as it is not used within the analysis.

The sense wires are read out by a set of cold electronics [7] which are submerged within the liquid argon at the top of the APAs. The cold electronics shape and amplify the incoming analog signals, which are then digitized at a rate of 2 MHz for processing by the data acquisition system. When a beam line trigger occurs, the data acquisition system captures 6000 consecutive samples (3 ms) from each wire channel, starting 500 samples (250 μs) before the trigger, to construct a single event.

B. H4-VLE beam line

ProtoDUNE-SP received charged particles from a low-energy extension of the H4 beam line called the H4-VLE beam line [8]. The beam instrumentation provides

[2]The directions are defined according to a right-handed coordinate system, where y points upward and z and x point horizontally. z is parallel to the anode planes.

ProtoDUNE-SP with event-by-event triggering, momentum reconstruction (using a spectrometer formed of multiple fiber planes which measure the deflection of beam particles by one of the beam magnets), and PID using time of flight and Cherenkov devices.

ProtoDUNE-SP collected data from e^+, p, K^+, π^+, and μ^+ in various mean-momentum settings in the range 0.3–7 GeV/c. This analysis made use of the π^+ and μ^+ events in 1 GeV/c momentum runs, which, while the beam line PID was able to separate positron and proton triggers from the π^+ and μ^+ triggers, were indistinguishable from each other within the beam line PID. The inability to distinguish these particles within the beam line PID had a negligible effect on the analysis, since most of the μ^+ tended to exit the fiducial volume used within the event selection described later on.

III. SIMULATION

Events are generated from incident test beam particles resulting from a dedicated G4Beamline [9] simulation of the 80 GeV/c H4 beam interacting with a 30 cm tungsten target using the FTFP_BERT Geant4 [10] physics list. The resulting particles are transported through the H4-VLE extension [8], and the interactions within the various H4-VLE instrumentation components are simulated. This produces a realistic set of particles which reach the detector and trigger the beam line instrumentation. Cosmic-ray particles are overlaid onto the beam events using the CORSIKA Monte Carlo (MC) simulation [11].

The set of beam and cosmic-ray particles is propagated within the detector volume and their interactions are simulated using Geant4 with the QGSP_BERT physics list implemented within LArSoft [12]. The hadronic interaction model within the QGSP_BERT physics is based on the Bertini intranuclear cascade model [13,14] with preequilibrium and evaporation models used below an incident hadron energy of roughly 200 MeV [15]. The ionization of the LAr by the transported charged particles, the subsequent drift of the ionization electrons, and the final detector readout are simulated within LArSoft. The simulation includes electric field nonuniformities, including those caused by the space charge effect [16] (SCE), to reproduce more realistically the distortions of the detector response observed in data [5]. We also include a simulation of the effect of the unpowered electron diverters, in which charge drifting near the gap between APAs is captured.

A. $\pi^{\pm}$-nucleus interaction modeling

We compare our results with several cascade models (Geant4 Bertini, Geant4 INCL++, and GENIE hN) and one effective model (GENIE hA). Cascade models share a core principle arising from the fact that, at incident energies relevant to this measurement, the de Broglie wavelengths of hadrons are of the same order as or less than the distance between nucleons within a nucleus. As such, individual particle-particle interactions may be simulated within the nucleus [17]. Particles are propagated through the nucleus, potentially interacting at each step. These interactions lead to further interactions in the nucleus, and so on, giving rise to a cascade of particles within the nucleus. Once all particles are either absorbed within or escape the nucleus, the cascade ends. Cascade models may differ in specific treatments of the cascades themselves (i.e. the nuclear environment and available constituent interactions) and in additional physics modeling employed to describe aspects of hadron-nucleus interactions outside of the scope of the cascade modeling (i.e. evaporation from excited nuclear states). The models are described as follows:

(1) *Geant4 Bertini cascade model*. This model is based on the intranuclear cascade model originally developed by Bertini [13,14]. The implementation within Geant4 is valid from energies of 200 MeV up to ∼10 GeV and includes preequilibrium physics, nuclear breakup, and evaporation. Below 200 MeV incident energies, the preequilibrium model is invoked [10].

(2) *Geant4 INCL++ cascade model*. This is based on a combination of the Liège cascade model [18] and a statistical deexcitation model [19,20]. Differences to the Bertini cascade model include the description of the nuclear medium, the set of available particle-particle interactions within the nucleus and the associated cross sections, as well as an upper limit on the duration (in time) of the cascade [17].

(3) *GENIE hN cascade model*. The full intranuclear cascade implemented within the GENIE neutrino event generator samples the angular distributions[3] as functions of energy for several reactions between free π, K, p, n, and γ, with adjustments to reflect the influence of the surrounding nuclear medium [22].

(4) *GENIE hA effective model*. Rather than fully simulating the interactions of individual particles within a nuclear cascade, this effective model uses the total cross section for each possible nuclear process for pions scattering off of iron as a function of energy up to 1.2 GeV. For nuclear targets other than iron, the cross sections are extrapolated by scaling by $A^{2/3}$.

IV. RECONSTRUCTION

Noise filtering, signal processing, and readout issue mitigation are performed on the electronic readout waveforms [5]. Algorithms identify "hits" representing individual charge depositions on the readout wires. The Pandora reconstruction software [23,24] then performs 2D and then 3D clustering of these hits to identify collections of charge

[3]The angular distributions come from partial wave analyses provided by the George Washington University group [21].

depositions arising from individual particles. Pandora also identifies the primary beam particle and its interaction vertex and builds the "tree" of particles produced from the interaction. A convolutional neural network [25] is used to classify the individual hits as resulting from either tracklike particles (i.e. protons, pions, muons) or showerlike particles (i.e. positrons). The reconstructed positions of individual hits are corrected from the distorted readout using data-driven SCE maps [16]. Following calibration and drift electron lifetime corrections, the recorded charge deposited per unit length, dQ/dX, of tracks is converted to energy lost per unit length dE/dX using estimates of the electric field strength within the modified box model [26] and these corrected positions [5,27].

V. METHODOLOGY

In order to measure the cross sections, events in data and from simulation are categorized according to the event selection described in Sec. V A. The simulated event distributions are parametrized and used within a binned likelihood fit to the data as described in Sec. V B. The best-fit parameters are used to create a varied set of simulated event distributions which best match the data. The cross sections are extracted from truth-level information of the best-fit MC using the thin-slice method developed by LArIAT [28]. We choose to segment the simulated primary π^+ tracks according to the collection plane wire pitch, though this segmentation is ultimately an arbitrary choice for our application of this method.

A. Event selection

The analysis made use of beam events which were categorized as π^+/μ^+ by the beam instrumentation by requiring no signal in the low-pressure Cherenkov device and a measured time of flight less than 110 ns [5] from all 1 GeV/c runs. Events with degenerate hits in any of the scintillating fiber planes of the momentum spectrometer were rejected to avoid ambiguities in momentum reconstruction.

The reconstructed beam momentum spectrum of the data was found to be wider than in MC. The shape difference was accounted for by normalizing MC to data in bins of reconstructed beam momentum. Due to low amounts of events in the tails, the reconstructed beam momentum region was restricted to $(750, 1250)$ MeV/c.

As explained in Ref. [29], preselection criteria were used to increase the purity and reconstruction quality of selected events. First, there must be a valid reconstructed primary particle: Pandora must have identified a cluster as coming from the beam and reconstructed that cluster as tracklike as opposed to showerlike. Second, the reconstructed beam track must have extended at least 30 cm (after SCE corrections) into the TPC in the z direction. Finally, a set of positional and directional cuts on the reconstructed beam track was used in order to reduce the number of cosmic rays or interactions upstream of the TPC which were misidentified as the primary beam particle.

The events passing this cut were then placed into one of the following four categories: escaping tracks, absorption candidates, charge exchange candidates, and other interaction candidates.

Escaping tracks are any reconstructed beam track which extended (without SCE corrections) at least 215 cm into the detector in the z direction. The location of this cut in z is chosen such that tracks which are distorted by the grounded electron diverters are not considered interaction candidates. Additionally, including this category in the fit helps to constrain both the relative number of μ^+ in the sample (since μ^+ are more likely to exit the fiducial volume) and the total inelastic cross section. This last point results from the fact that π^+ will be more (less) likely to travel past this cut in z if their total cross section is lower (higher). Note that this does limit the efficiency of selecting low-kinetic-energy interactions, leading to the restricted low end of the measurement range (500–800 MeV).

Reconstructed beam tracks that end before the previous cut in z are all considered interaction candidates and are further separated into the three signal interactions (as described in Sec. I). This is achieved by using the reconstructed particles that are associated with the interaction products of the primary reconstructed beam track. A reconstructed interaction product is given a charge-weighted tracklike score T as defined in Eq. (1),

$$T = \frac{1}{Q}\sum_{i}^{N_{\text{Hits}}} t_i q_i; \qquad Q = \sum_{i}^{N_{\text{Hits}}} q_i, \tag{1}$$

where t_i and q_i are the track score from the aforementioned convolutional neural network and integrated charge of each hit on the collection plane, respectively, and Q is the total charge deposited on the collection plane for the given reconstructed cluster. We use the charge-weighted score because it yields better agreement between data and simulation in this analysis compared to simply summing individual scores and normalizing over the number of hits. For the same reason, the sum is restricted to hits on the collection plane.

The dE/dX of reconstructed tracks is then used to identify $\pi^\pm$ candidates. Candidates for γ resulting from the decay of secondary π^0's are identified using the energy of the shower and the distance between the end of the beam track and the start of the shower. If a primary beam track has no $\pi^\pm$ candidates and no γ candidates in its set of interaction products, it is considered an absorption event. If it has no $\pi^\pm$ candidates and at least one γ candidate, it is

TABLE I. Efficiencies and purities of the event selection. Note that the first two columns are relative to the events that pass the preselection, while the third column is relative to the entire simulation sample.

Channel	Efficiency (%)	Purity (%)	Overall efficiency (%)
Absorption	63	63	36
Charge exchange	42	75	20
Other	69	63	31

considered charge exchange. Finally, if it has at least one $\pi^{\pm}$ candidate, it is considered an "other" interaction.

The resulting purities (the number of true interaction events selected as that interaction divided by the number of true interactions of that type) and efficiencies (the number of interactions of any true category selected as a given interaction candidate divided) within the set of events passing the preselection are shown in Table I. The "overall efficiency"—in which the denominator also includes events failing the preselection—is also shown. The true interactions and selection efficiencies (relative to preselection) as functions of π^+ kinetic energy are shown in Fig. 2. Example candidates for the three signal interactions are shown in Fig. 3.

The selected distributions resulting from the prefit MC (after normalizing according to the reconstructed beam line momentum distribution in data) are shown in Fig. 4 and are broken down by category from MC information: the three signal interactions, beam muons, pions which interacted upstream of the TPC active volume, pions which exited the fiducial volume, and pions which stopped or decayed within the fiducial volume. Distributions collected from data are superimposed on the MC distributions. The absorption, charge exchange, and other interactions are binned according to the reconstructed kinetic energy at the identified interaction point. This is calculated by subtracting the primary pion track's total deposited energy from the kinetic energy reconstructed within the beam line. Events in which the reconstructed beam track extended past the limit in z are contained in a single bin as shown in Fig. 4(d). We observe several differences between data and simulation in the shape and magnitude of several distributions. The observed differences are consistent with coming from two effects: (i) the number of interactions upstream of the active volume of the TPC and (ii) differences in the cross sections for the signal interactions here. As will be described later, we account for the first during the fit to data using a nuisance parameter and intend to measure the differences in physics resulting from the second point.

B. Fitting strategy

The MC simulation is fit to the observed data in order to estimate the number of interactions as a function of the pion kinetic energy at the point of interaction. A binned likelihood fit is performed in which the fit parameters include a set of signal parameters which scale the number of signal events (absorption, charge exchange, and other inelastic interactions of primary beam π^+) in bins of true kinetic energy at interaction. These true kinetic energy bins are 100 MeV in width and range from 500 to 800 MeV for each channel. These nine bins form the set of measurement bins within this analysis. Their widths were chosen according to the resolution of the energy reconstruction for these events. The total range (500–800 MeV) was chosen according to where the selection efficiency begins to fall off as function of kinetic energy. Scaling parameters are also applied to the underflow and overflow regions for the three channels, though the cross sections are not measured in these regions. A parameter that scales the number of interactions between the end of the beam line and the beginning of the TPC volume is included.

During each step of the fit, after the fit parameters are applied to the MC events, the MC events are reweighted according to the momentum distribution in data as reconstructed by the beam line instrumentation as described

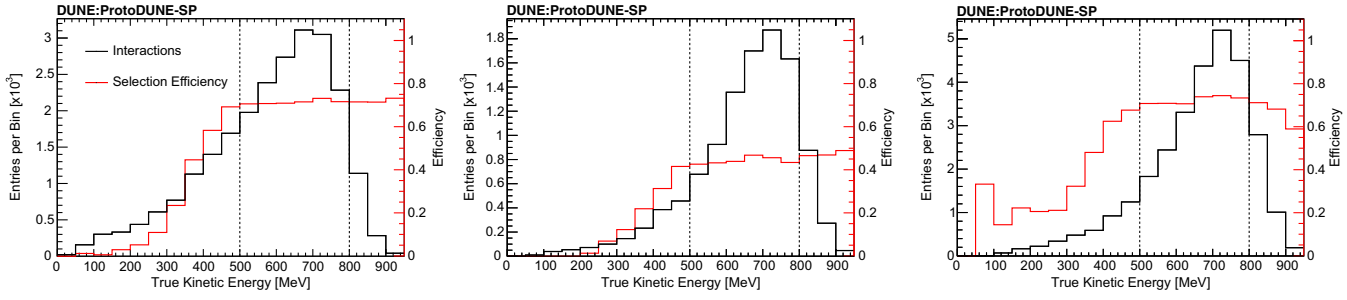

(a) Absorption (b) Charge Exchange (c) Other Interactions

FIG. 2. True interaction distributions (black) and selection efficiencies (red—relative to the events that pass preselection) for the three signal interactions measured in this analysis. The bounds of the measurement range are shown as the dashed vertical lines.

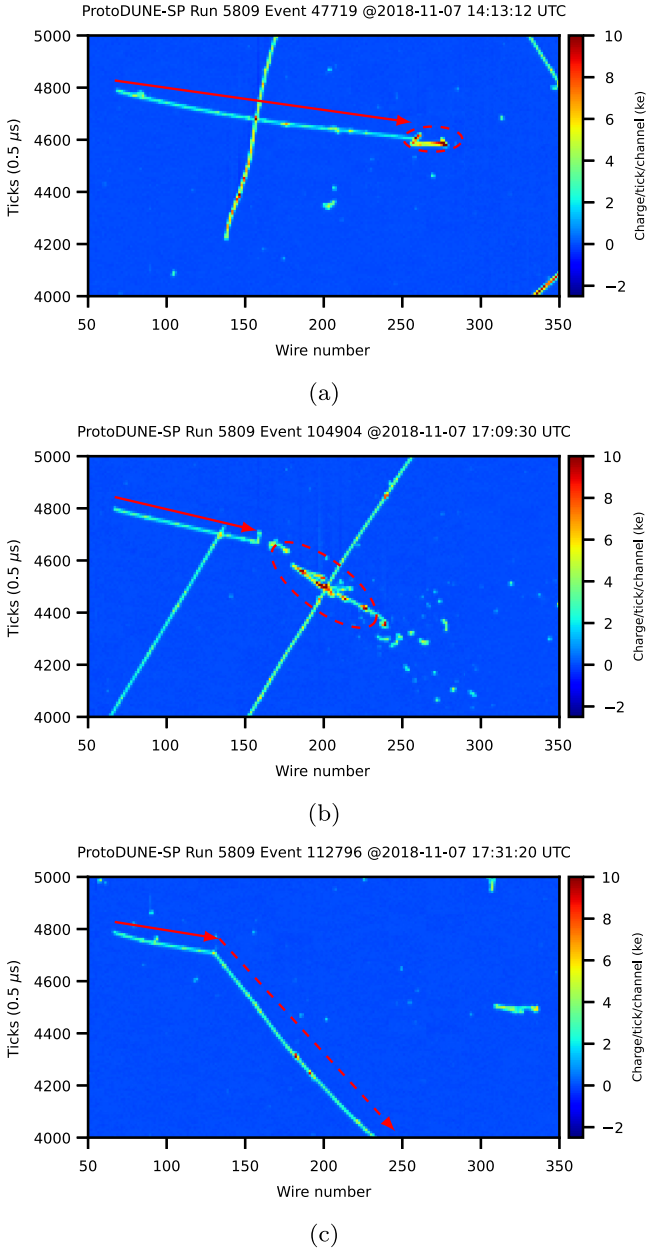

FIG. 3. Event displays of selected interaction candidates for π^+-argon absorption (a), charge exchange (b), and other (c) interactions using the event selection described in Sec. VA. The candidate beam pion tracks begins near wire 60, tick 4800 (reconstructed at roughly $x = -24$ cm and $z = 1$ cm after SCE corrections) and travels toward the bottom right of each figure, as highlighted by the solid, red arrow. The dashed ellipse in (a) highlights two proton candidate tracks, and in (b) it highlights a candidate γ resulting from a π^0 decay. In (c), the secondary $\pi^{\pm}$ is highlighted with a dashed arrow. Candidate cosmic-ray tracks can be seen crossing through the figures as well.

previously in Sec. VA. This is done such that the primary change to the simulation is the rate of interactions at various energies rather than changing the initial momentum distribution.

The fit minimizes the negative log-likelihood ratio:

$$-2\log(\lambda) = 2\sum_j \left(\beta_j N_j^{\mathrm{MC}} - N_j + N_j \log\frac{N_j}{\beta_j N_j^{\mathrm{MC}}} + \frac{(\beta_j - 1)^2}{2\sigma_j^2}\right). \quad (2)$$

Equation (2) is derived from the Poisson likelihood to observe N_j events in the set of reconstructed bins j in which $\beta_j N_j^{\mathrm{MC}}$ events are predicted. β_j are scaling factors proposed by Barlow and Beeston which account for MC statistical uncertainty and reflect the fact that the generated MC events N_j^{MC} are themselves drawn from some underlying distribution with mean $\beta_j N_j^{\mathrm{MC}}$ [30]. Barlow and Beeston treat these factors as additional nuisance parameters in the fit. However, we follow Conway's treatment [31], in which a Gaussian constraint[4] is added to the likelihood and the factors are determined analytically by setting the derivative of the likelihood with respect to each β_j to 0 (maximizing the likelihood).

C. Iterative fit procedure

In order to mitigate any dependence of the analysis results on the choice of signal model, we developed an iterative fit procedure. In each subsequent fit, the signal model is updated using Geant4Reweight [32] which produces event weights to effectively modify the π^+ cross sections in the input MC to match the cross sections extracted from the previous fit.

Tests were performed using fake data produced from MC varied by Geant4Reweight in order to verify the convergence of this technique. The fake data was produced by reweighting the signal cross sections by 10%–50%, binning the reweighted MC, and then statistically fluctuating these distributions to approximate statistical independence between the fake data and input MC. This procedure reduces the bias to less than 1% of the true cross sections. This residual bias is negligible compared to the systematic uncertainties. Additionally, a data-driven stopping criterion was developed as follows. For a given set of data (fake or real), we fit to 500 statistically varied distributions drawn from the dataset. For each of these fits, the result is used to update the model, and the fit is performed again using the update. We calculate the χ^2 between each updated fit and its previous iteration, using the distribution of extracted cross sections values from the updated iteration to calculate the covariance used within the χ^2 calculation. This χ^2 represents how much the model continues to change in each subsequent fit. We continue updating and refitting until 90% of fits end with $\chi^2 < 1$

[4]With variance $\sigma_j^2 = \sum_i w_i^2/(\sum_i w_i)^2$. w_i is the weight of event i in bin j. The sums run over each event in bin j.

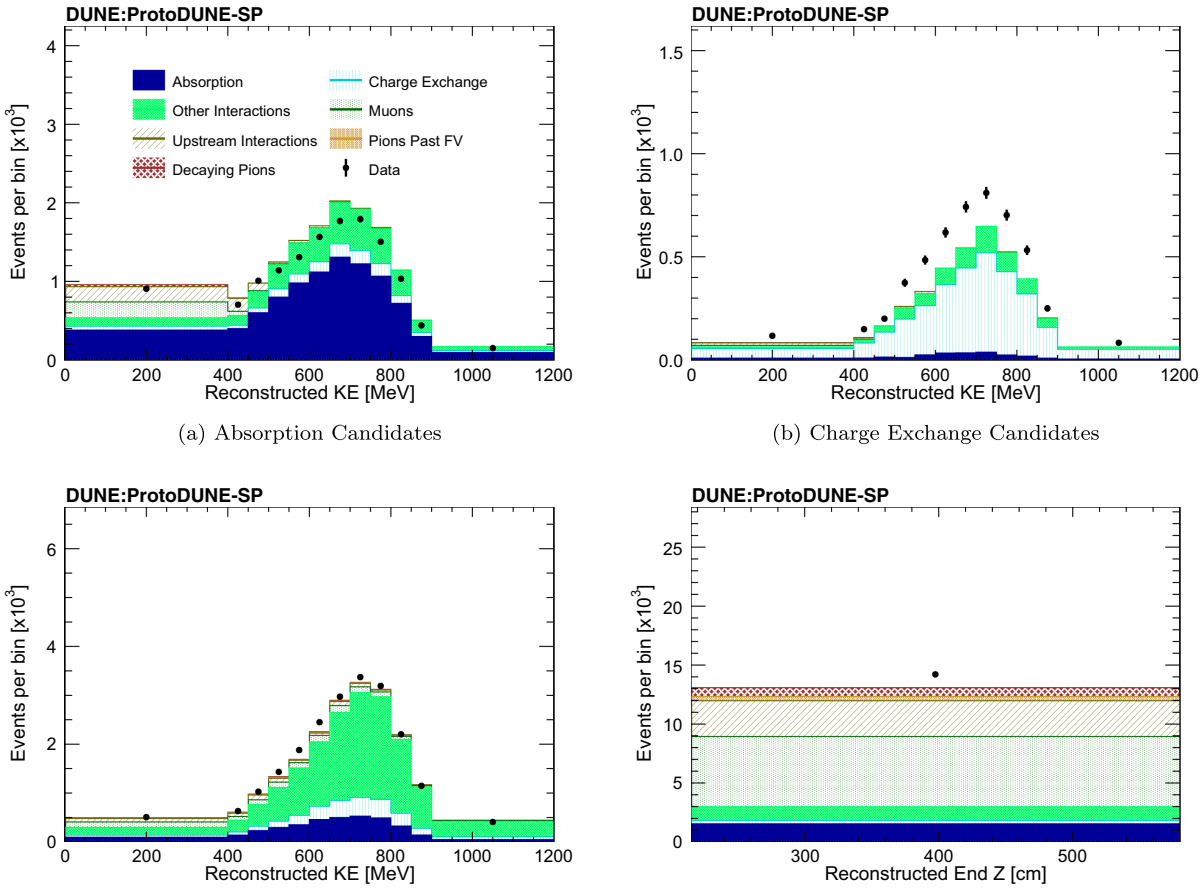

(a) Absorption Candidates

(b) Charge Exchange Candidates

(c) Other Interaction Candidates

(d) Escaping Tracks

FIG. 4. Selected event distributions from the ProtoDUNE-SP MC with stacked contributions broken down by true event category. These categories are (i) the three signal pion interactions—absorption, charge exchange, and other interactions; (ii) primary muons; (iii) primary beam pions which interacted before reaching the TPC active volume (i.e. within the beam plug); (iv) pions which extended past the fiducial volume (FV); and (v) pions which decayed within the FV (either in flight or after stopping). Also shown are the selected event distributions observed in data (black points). The error bars shown for the data are the estimated statistical uncertainties on the selected event rate.

indicating that the model has stopped updating. In the case of this measurement, we stopped iterating at the fourth fit. The differences between the cross sections from the first and fourth fit to data relative to the fourth-fit cross sections are shown in Table II.

TABLE II. Differences between the cross sections from the first and fourth iterations of the fit to data relative to the cross section from the fourth fit iteration for each π^+ kinetic energy bin.

	Relative difference		
T_π [MeV]	Absorption (%)	Charge exchange (%)	Other interactions (%)
550	−7.1	+11.2	+8.3
650	−3.8	+5.0	+5.2
750	−4.6	+2.6	+3.7

VI. TREATMENT OF UNCERTAINTIES

In order to propagate uncertainties within the analysis, alternate fits are performed by varying either some aspect of the simulation or, in one case, the calibration in data for each uncertainty source. These alternate cross sections are used to calculate covariances which are added in quadrature to give the full covariance of the measured cross sections.

For the statistical uncertainty associated with the collected data, alternate datasets are generated by setting the number of events in each bin of data to Poisson-distributed random integers drawn from the content of each bin. The simulation is then fit to these alternate datasets, and the contribution to the covariance of bins i and j is calculated as

$$V_{ij} = \frac{1}{N_{\text{Fits}}} \sum_{k}^{N_{\text{Fits}}} (\sigma_i - \sigma_i^k)(\sigma_j - \sigma_j^k). \tag{3}$$

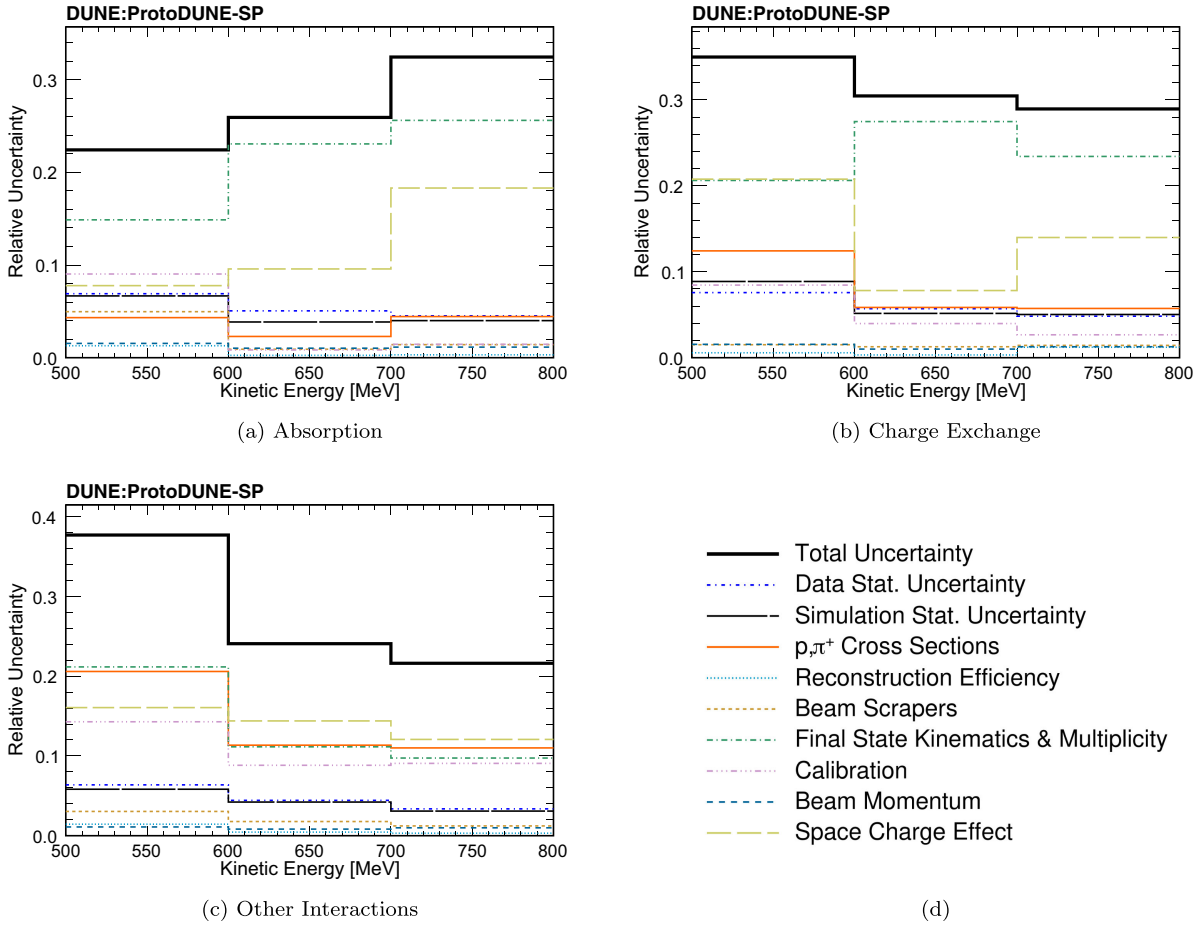

FIG. 5. Uncertainties relative to the best-fit cross section values for absorption (a), charge exchange (b), and other interactions (c). The total uncertainty is shown as the solid black line, and the uncertainty contributions are shown in the various colors and line styles. The uncertainty contributions added in quadrature equals the total uncertainty. The legend is shown in (d) and reflects the different sources described in Sec. VI.

Here, $\sigma_{i(j)}$ is the cross section in true bin i (j) from the "standard" (simulation and collected data) fit result and $\sigma^k_{i(j)}$ is the cross section in true bin i (j) from the kth alternate fit. We performed fits to $N_{\text{Fits}} = 500$ statistically varied distributions.

A similar procedure is performed for the statistical uncertainty associated with the input simulation. However, instead of changing the data distributions, the simulation distributions were varied by producing event weights calculated by drawing Poisson-distributed numbers around the number of events in the initial simulation distributions. The covariances are calculated again using Eq. (3), and we used the same number of varied fits for the calculation. The number of events from our simulation is of the same order as those in the data; the statistical uncertainties are thus very similar. Future analyses will make use of a larger sample of input simulation to reduce this uncertainty.

The individual systematic uncertainties are described below, and their contribution to the uncertainty of the measurement is shown in Fig. 5. The label by which the systematic effect is referred to within this figure is stated at the end of each item. Unless otherwise stated, their contributing covariances in bin (i, j) are calculated from fits using simulation varied with $\pm 1\sigma$ shifts to the underlying effect and are given by

$$V_{ij} = \frac{1}{2}((\sigma_i - \sigma_i^+)(\sigma_j - \sigma_j^+) + (\sigma_i - \sigma_i^-)(\sigma_j - \sigma_j^-)), \tag{4}$$

where $\sigma^{\pm}$ represents the cross section extracted from the fit with the systematic effect varied by $\pm 1\sigma$. Several of the systematic effects described below are broken up into multiple independent contributions to the total uncertainty. In other words, when specified, several independent variations to the fit—and thus separate covariances calculated as in Eq. (4)—have been made. In these cases, the corresponding uncertainty contributions in Fig. 5 include these separate covariances added in quadrature.

(1) Beam scrapers: the number of beam π^+/μ^+ that scrape along the beam plug between the end of the beam line and the beginning of the active TPC volume. The beam plug displaces argon along the nominal path of the beam particle so less energy is lost and fewer hadronic interactions occur before the beam particle enters the active volume of the TPC. A difference in the number of particles which scrape the plug can affect the relationship between true and reconstructed π^+ energy at interaction. Simulation showed that the distributions in momentum of the beam π^+/μ^+ differ due to the fact that some of the muons originate from decaying pions. The effect was parametrized separately for pions across their momentum range and for two regions in the momentum range of beam muons (corresponding to different populations of muons which were produced from hadron decays at different points along the beam line). A 50% uncertainty to the number of scraping particles in each of these three populations was estimated.

(2) p, π^+ cross sections: the total interaction rate of π^+ and protons. A misestimation of the inelastic cross sections can affect selection efficiencies and purity. As such, event weights were produced using Geant4Reweight [32] to represent variations to the proton and π^+ cross sections. One parameter was used to vary the proton cross section across a momentum range encompassing all protons produced within the MC sample. Two parameters were used for π^+ interactions: (i) below 600 MeV/c and (ii) above 600 MeV/c pion momentum. A 33% uncertainty was assigned to the cross section parameters and was estimated from the spread of various hadron-nucleus interaction models. The separation of the systematic effect for π^+ into two momentum regions was informed by the varying final state behavior between the models [2].

(3) Final state kinematics and multiplicity: final state kinematics and multiplicities of the primary interaction. The selection efficiency can depend on the distribution in various dimensions of phase space of final state particles emitted from the primary interactions. By comparing to either GENIE's hA/hN models or Geant4's INCL++ hadronic interaction model, two alternate simulation sets were produced for each of the following projections:
   (a) momentum of the leading outgoing p,
   (b) momentum of the leading outgoing π^+,
   (c) momentum of the leading outgoing π^0,
   (d) angle (relative to the primary π^+) of the leading p,
   (e) angle of the leading π^+,
   (f) angle of the leading π^0,
   (g) p multiplicity,
   (h) n multiplicity,
   (i) π^+ multiplicity,
   (j) π^- multiplicity, and
   (k) π^0 multiplicity.

Of these, the largest effects come from p and n multiplicities as well as the leading p angle and momentum. The corresponding uncertainty for this effect as shown in Fig. 5 includes all of the projections above added together in quadrature.

(4) Reconstruction efficiency: beam reconstruction and matching efficiencies. Systematic effects arise in reconstruction due to differences between data and MC in the incident beam's direction and position on the face of the detector. Two parameters were implemented to account for these effects. The first varies the efficiency of reconstructing tracks to beam particles with short true trajectory length (defined as less than 30 cm), while the second varies the rate of Pandora's ability to correctly choose the true test beam particle itself as the reconstructed beam rather than choosing a cosmic-ray particle as the beam. For the former, we performed a study using selected beam tracks, wherein the tracks were artificially shortened by removing reconstructed hits from the event record. From this, we observed a 26% difference between data and MC performance in the ability to correctly reconstruct these shortened tracks, and we used this value as the uncertainty on the effect. For the second effect, we used a conservative 100% relative uncertainty on the rate of misidentification.

(5) Beam momentum: differences in the relationship between momentum reconstructed by the spectrometer in the beam line and the true momentum at the beginning of the TPC active volume can lead to a different smearing between true and reconstructed energy at π^+ interaction—one of the primary observables in the fit. This relationship was found to be described by a second-order polynomial, and a sample of stopping beam particles was used to determine the covariance between this polynomial's coefficients. 500 alternate simulation sets were produced by sampling these coefficients. These alternate sets were fit to data, and the covariance was calculated as in Eq. (3).

(6) Calorimetry calibration: an integral part of the calibration is determining the overall charge scale of the detector. This is used in converting a track's dQ/dX (charge reaching the readout wires per unit length) into its dE/dX (energy deposited per unit length). A 3% uncertainty was assigned to the overall charge scale factor used within the dQ/dX to dE/dX conversion (a slightly more conservative value according to the study performed in Ref. [5]).

(7) Space charge effect: as in Ref. [29], studies using a sample of cosmic ray tracks found an 8% uncertainty

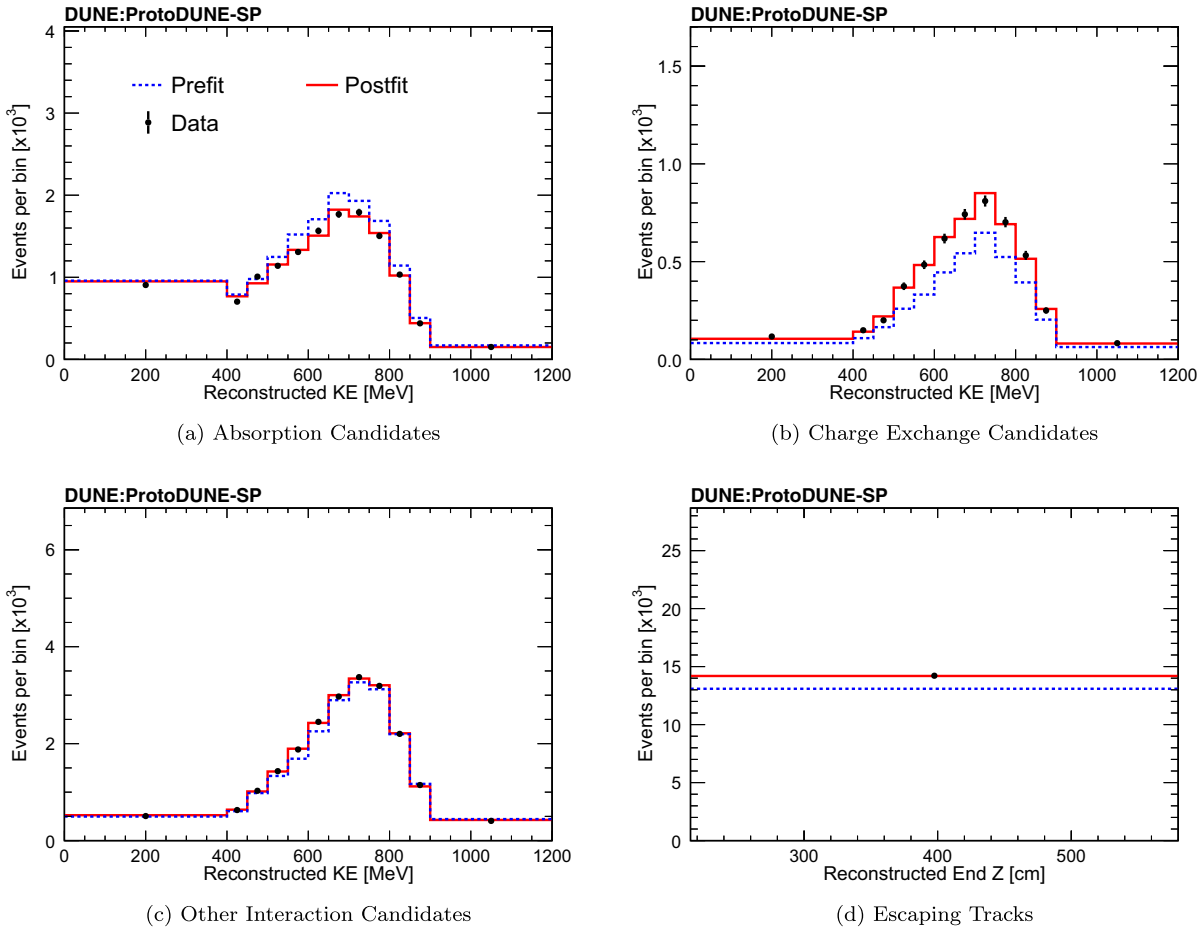

(a) Absorption Candidates

(b) Charge Exchange Candidates

(c) Other Interaction Candidates

(d) Escaping Tracks

FIG. 6. Event distributions observed by ProtoDUNE-SP (black circles) compared to prefit (dashed blue histogram) and postfit MC (solid red histogram) using four fit iterations. The error bars on the bins of the data distribution (often smaller than the data point markers themselves) represent the estimated statistical errors.

on the magnitude of spatial distortions arising due to SCE. Alternate MC samples were produced where the distortions were increased or decreased by 8% and used to fit the standard dataset.

The individual covariances (V_{ij}) from the aforementioned sources (data-statistical, MC-statistical, and systematic effects) are added in quadrature to give the full covariance of this analysis.

VII. RESULTS

Figure 6 shows reconstructed event distributions collected in data and as predicted by the prefit and postfit MC (for which our data-driven iterative extraction procedure ran for four iterations) in the various samples described in Sec. V A. The distributions show good agreement between the postfit MC and data.

As mentioned earlier, the cross sections are calculated from the best-fit MC truth information using a "thin-slice" calculation. This is necessary because our target is the extended volume of the LAr and not a thin target as in other scattering experiments. For every primary π^+ that reaches the start of our fiducial volume, we determine if it interacts before the end of the fiducial volume and, if so, its type of interaction and the kinetic energy at which it interacts. We bin these events in three "interaction histograms" using weights from the best-fit MC and with the same binning ranges used for the fit (500–600, 600–700, 700–800 MeV). Additionally, we construct an "incident histogram" with the same binning. For our measurement, this is analogous to the flux used within a thin-target experiment. This is done by artificially segmenting the trajectories of the true π^+ within our fiducial volume. The choice of coarseness of this segmentation is—to an extent—arbitrary. As a "natural choice," we segment the trajectories using the collection-plane wire spacing. We find the kinetic energy of the π^+ as it enters into a new slice and fill the incident histogram using the same event weights as before. This is done up to the point of interaction, and so any given event can contribute multiple times to the incident histogram. Following this procedure, we are left with four distributions: one for each of the three interactions and one for flux

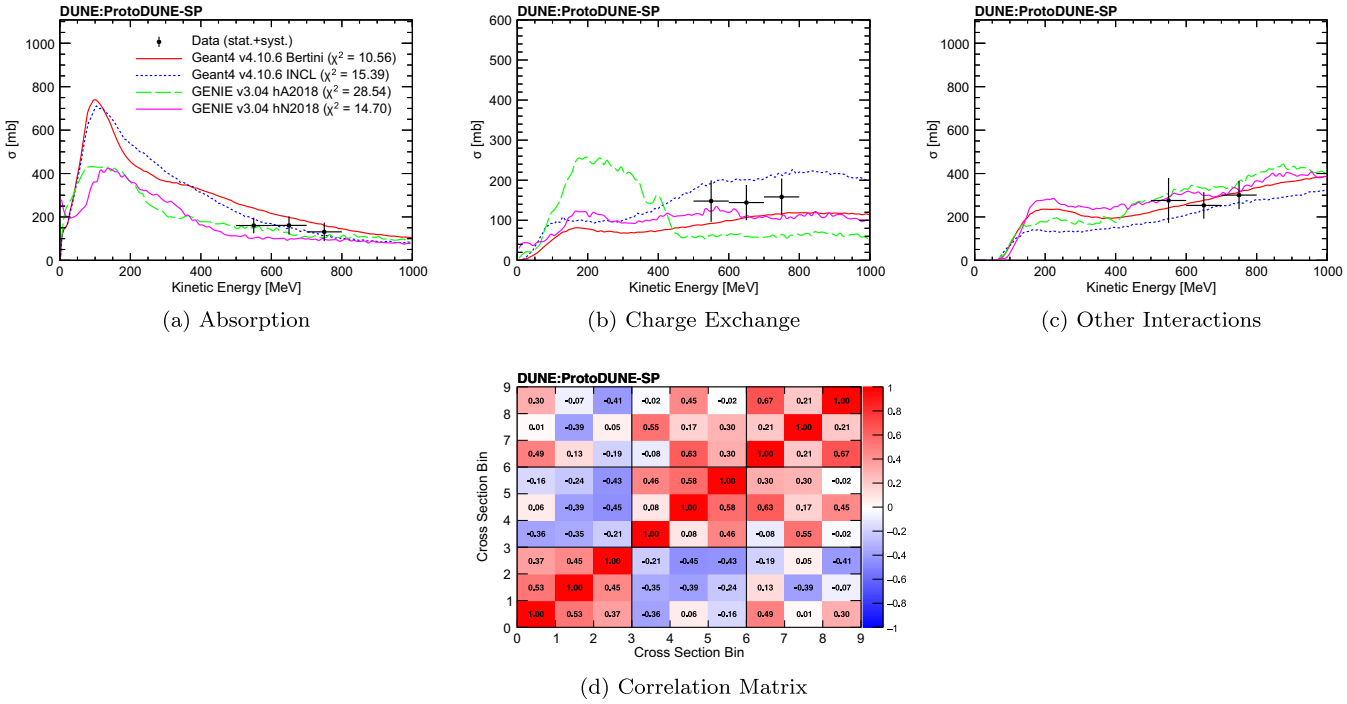

(a) Absorption (b) Charge Exchange (c) Other Interactions

(d) Correlation Matrix

FIG. 7. ProtoDUNE-SP measurement of the cross sections for absorption (a), charge exchange (b), and other interactions (c) compared to Geant4 and GENIE predictions. The error bars represent the combined statistical and systematic uncertainties (added in quadrature). (d) shows the correlations between the measured cross sections. The bins are arranged as: absorption (1, 2, 3), charge exchange (4, 5, 6), and other (7, 8, 9) in order of increasing kinetic energy. The black lines are guides to highlight the sections of the correlation matrix representing different exclusive channels. The χ^2 shown in (a) are calculated using the nine bins across the three channels and their covariances.

contributions. These are summarized in Table III. For a given interaction type l and within a given kinetic energy bin, the cross section (σ^l) can be calculated using these distributions within the following equation:

$$\sigma^l = \frac{M_{\mathrm{Ar}}}{N_{\mathrm{A}}\rho t}\ln\left(\frac{N_{\mathrm{inc}}}{N_{\mathrm{inc}} - N^l_{\mathrm{int}}}\right), \tag{5}$$

TABLE III. Values used within the thin-slice cross section calculations for each π^+ kinetic energy bin extracted from the best-fit MC. The first column denotes the center of the kinetic energy bin as T_π. The second, third, and fourth columns are the number of interactions of the three exclusive signal channels. The far right column is the number of incident entries. For brevity, and because the correlations between these values are nontrivial, we only report the best-fit values and omit the uncertainties.

T_π [MeV]	$N^{\mathrm{Abs}}_{\mathrm{int}}$	$N^{\mathrm{Cex}}_{\mathrm{int}}$	$N^{\mathrm{Other}}_{\mathrm{int}}$	N_{inc}
550	2433	2242	4179	1443×10^3
650	4127	3696	6484	2440×10^3
750	5207	6281	11921	3777×10^3

where N^l_{int} is the number of interactions of type l, N_{inc} is the number of incident entries in this energy range,[5] $M_{\mathrm{Ar}} = 39.948$ g/mol is the atomic mass of argon, $\rho = 1.4$ g/cm^3 is the density of liquid argon, N_{A} is Avogadro's number, and $t = 0.498$ cm is the thickness of the slices used for segmentation.[6]

Figure 7 shows the exclusive cross sections measured within this analysis in comparison to those predicted by the Bertini and INCL cascade models within Geant4 [17] as well as the GENIE FSI models hA and hN [22]. The model predictions shown in Fig. 7 include the signal definition restrictions used in the analysis, wherein charged pions less than 150 MeV/c momentum may be included within the final states of absorption and charge exchange, and multiple π^0's can be present in charge exchange. Figure 7(d) shows the correlations between cross section bins defined as $c_{ij} = \frac{v_{ij}}{\delta_i \delta_j}$. Here, v_{ij} is the covariance between bins i and j, and $\delta_{i(j)}$ is the square root of the variance of bin i (j) and is shown as the error bars in Figs. 7(a)–7(c). The χ^2 shown in Fig. 7(a) is defined as $\chi^2 = (\vec{\sigma} - \vec{\sigma}_{\mathrm{pred}})^T V^{-1} (\vec{\sigma} - \vec{\sigma}_{\mathrm{pred}})$,

[5]Note: this is common across all three interactions.

[6]This is given by the wire spacing of the collection plane (0.4974 cm) along with a factor of 1.039 to account for the angle of the beam relative to the wires.

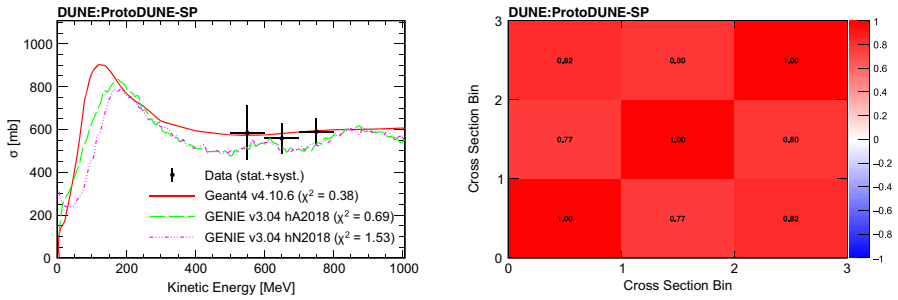

(a) Total Inelastic Cross Section (b) Correlation Matrix

FIG. 8. (a) ProtoDUNE-SP measurement of the total cross section compared to Geant4 and GENIE predictions. (b) shows the correlations between the data points shown here in order of increasing kinetic energy.

TABLE IV. Summary of cross section results for each π^+ kinetic energy bin. The first column denotes the center of the kinetic energy bin as T_π. The second, third, and fourth columns are the three exclusive signal channels. The far right column is the total inelastic cross section.

T_π [MeV]	σ_{Abs} [mb]	σ_{Cex} [mb]	σ_{Other} [mb]	σ_{Tot} [mb]
550	160 ± 36	148 ± 52	276 ± 104	584 ± 127
650	161 ± 42	144 ± 44	253 ± 61	558 ± 70
750	131 ± 43	158 ± 46	301 ± 65	590 ± 64

where $\vec{\sigma}$ are the measured cross sections, $\vec{\sigma}_{\text{pred}}$ are the predicted cross sections in question, and V^{-1} is the inverted covariance matrix. Table IV summarizes the measured cross sections and their variances.

Of the models shown here, the data are consistent with the Bertini cascade and INCL++ models from Geant4 as well as GENIE's *hN* model, with a slight preference for the Bertini cascade ($p \approx 0.31$, 0.08, and 0.10, respectively).[7] Meanwhile, GENIE's *hA* model is inconsistent with these data ($p < 0.001$). This is not surprising, as *hA* is an effective model rather than a full intranuclear cascade model like the other models.

We also present the total inelastic cross section in Fig. 8 calculated by summing the measured exclusive cross sections. It is important to stress that this measurement of the total cross section is not independent from the measurement of the three exclusive channels but is statistically valid for stand-alone comparisons to predicted total inelastic π^+ cross sections. The covariance matrix of the total cross section is calculated as

$$V_{ij} = \sum_{\mu}^{\{a,b,c\}} \sum_{\nu}^{\{a,b,c\}} v_{\mu_i \nu_j}, \tag{6}$$

where V_{ij} is the covariance of bins i and j in the total cross section. $v_{\mu_i \nu_j}$ is the covariance between bin i of exclusive channel μ and bin j of exclusive channel ν. The correlation matrix shown in Fig. 8(b) is defined as $C_{ij} = \frac{V_{ij}}{\Delta_i \Delta_j}$, where the variance Δ_i is the ith element of the diagonal of V. As can be seen, the bins of the measured total inelastic cross section are highly correlated.

We compare the total inelastic cross section to predictions from Geant4 and GENIE's *hA* and *hN* models in Fig. 8(a). Note that only one Geant4 prediction is shown, as the total cross section is out of scope of the Bertini and INCL cascade models (they only provide the dynamics of inelastic pion scattering interactions, not the rate at which the scattering occurs [17]). Again, the Geant4 prediction agrees best with the data, though each model is consistent with the data as indicated by the χ^2 values shown in the figure. A dedicated analysis on the total inelastic cross section using a different method was also performed, and the results from the total inelastic analysis are consistent with the combined cross sections presented here [33].

VIII. CONCLUSIONS

We have measured the absorption, charge exchange, and remaining inelastic π^+-argon cross sections using data taken by the ProtoDUNE-SP detector. This analysis showcases the capability of the DUNE LArTPC detector technology to perform particle tracking, identification, and energy reconstruction. This measurement will provide necessary inputs for the simulation used by DUNE and will improve the modeling of pions undergoing final state interactions within the nucleus as well as secondary interactions with the LAr volume of the DUNE detectors following a neutrino interaction. It is the first ever measurement of π^+-argon charge exchange and the first measurement of absorption on argon at the kinetic energy range of 500–800 MeV.

ACKNOWLEDGMENTS

The ProtoDUNE-SP detector was constructed and operated on the CERN Neutrino Platform. We gratefully

[7]Nine degrees of freedom are used within the χ^2 calculations.

acknowledge the support of the CERN management, and the CERN EP, BE, TE, EN and IT Departments for NP04/ProtoDUNE-SP. This document was prepared by DUNE Collaboration using the resources of the Fermi National Accelerator Laboratory (Fermilab), a U.S. Department of Energy, Office of Science, Office of High Energy Physics HEP User Facility. Fermilab is managed by Fermi Forward Discovery Group, LLC, acting under Contract No. 89243024CSC000002. This work was supported by CNPq, FAPERJ, FAPEG and FAPESP, Brazil; CFI, IPP and NSERC, Canada; CERN; MŠMT, Czech Republic; ERDF, Horizon Europe, MSCA and NextGenerationEU, European Union; CNRS/IN2P3 and CEA, France; INFN, Italy; FCT, Portugal; NRF, South Korea; Generalitat Valenciana, Junta de Andalucía-FEDER, MICINN, and Xunta de Galicia, Spain; SERI and SNSF, Switzerland; TÜBİTAK, Turkey; The Royal Society and UKRI/STFC, United Kingdom; DOE and NSF, USA. This research used resources of the National Energy Research Scientific Computing Center (NERSC), a U.S. Department of Energy Office of Science User Facility operated under Contract No. DE-AC02-05CH11231.

DATA AVAILABILITY

The data that support the findings of this article are openly available [34].

[1] B. Abi *et al.* (DUNE Collaboration), Volume I. Introduction to DUNE, J. Instrum. **15**, T08008 (2020).
[2] E. S. P. Guerra *et al.*, Using world $\pi^{\pm}$-nucleus scattering data to constrain an intranuclear cascade model, Phys. Rev. D **99**, 052007 (2019).
[3] K. Abe *et al.*, Measurements of neutrino oscillation parameters from the T2K experiment using 3.6×10^{21} protons on target, Eur. Phys. J. C **83**, 782 (2023).
[4] A. A. Abud *et al.*, Deep Underground Neutrino Experiment (DUNE) near detector conceptual design report, Instruments **5**, 31 (2021).
[5] B. Abi *et al.*, First results on ProtoDUNE-SP liquid argon time projection chamber performance from a beam test at the CERN neutrino platform, J. Instrum. **15**, P12004 (2020).
[6] A. A. Abud *et al.*, Design, construction and operation of the ProtoDUNE-SP liquid argon TPC, J. Instrum. **17**, P01005 (2022).
[7] D. Adams *et al.*, The ProtoDUNE-SP LArTPC electronics production, commissioning, and performance, J. Instrum. **15**, P06017 (2020).
[8] A. C. Booth, N. Charitonidis, P. Chatzidaki, Y. Karyotakis, E. Nowak, I. Ortega-Ruiz, M. Rosenthal, and P. Sala, Particle production, transport, and identification in the regime of 1–7 GeV/c, Phys. Rev. Accel. Beams **22**, 061003 (2019).
[9] T. J. Roberts, K. B. Beard, D. Huang, S. Ahmed, D. M. Kaplan, and L. K. Spentzouris, G4Beamline particle tracking in matter-dominated beam lines, Conf. Proc. C **0806233**, WEPP120 (2008), https://inspirehep.net/literature/795221
[10] S. Agostinelli *et al.*, Geant4—A simulation toolkit, Nucl. Instrum. Methods Phys. Res., Sect. A **506**, 250 (2003).
[11] D. Heck, J. Knapp, J. N. Capdevielle, G. Schatz, and T. Thouw, CORSIKA: A Monte Carlo code to simulate extensive air showers, Report No. FZKA 6019 (1998).
[12] E. D. Church, LArSoft: A software package for liquid argon time projection drift chambers, arXiv:1311.6774.
[13] M. Guthrie, R. Alsmiller, and H. Bertini, Calculation of the capture of negative pions in light elements and comparison with experiments pertaining to cancer radiotherapy, Nucl. Instrum. Methods **66**, 29 (1968).
[14] H. W. Bertini and M. P. Guthrie, News item results from medium-energy intranuclear-cascade calculation, Nucl. Phys. **A169**, 670 (1971).
[15] D. Wright and M. Kelsey, The Geant4 Bertini cascade, Nucl. Instrum. Methods Phys. Res., Sect. A **804**, 175 (2015).
[16] P. Abratenko *et al.*, Measurement of space charge effects in the MicroBooNE LArTPC using cosmic muons, J. Instrum. **15**, P12037 (2020).
[17] *Geant4 Physics Reference Manual, Version 10.6* (2019), https://geant4-userdoc.web.cern.ch/UsersGuides/PhysicsReferenceManual/BackupVersions/V10.6/html/index.html
[18] D. Mancusi, A. Boudard, J. Cugnon, J.-C. David, P. Kaitaniemi, and S. Leray, Extension of the Liège intranuclear-cascade model to reactions induced by light nuclei, Phys. Rev. C **90**, 054602 (2014).
[19] A. Kelic, M. V. Ricciardi, and K.-H. Schmidt, ABLA07—Towards a complete description of the decay channels of a nuclear system from spontaneous fission to multifragmentation, in *Joint ICTP-IAEA Advanced Workshop on Model Codes for Spallation Reactions* (2009), arXiv:0906.4193.
[20] A. Ershova *et al.*, Role of deexcitation in the final-state interactions of protons in neutrino-nucleus interactions, Phys. Rev. D **108**, 112008 (2023).
[21] R. A. Arndt, W. J. Briscoe, I. I. Strakovsky, and R. L. Workman, Extended partial-wave analysis of πN scattering data, Phys. Rev. C **74**, 045205 (2006).
[22] C. Andreopoulos, C. Barry, S. Dytman, H. Gallagher, T. Golan, R. Hatcher, G. Perdue, and J. Yarba, The GENIE neutrino Monte Carlo generator: Physics and user manual, arXiv:1510.05494.
[23] J. S. Marshall and M. A. Thomson, The Pandora software development kit for pattern recognition, Eur. Phys. J. C **75**, 439 (2015).

[24] A. Abed Abud *et al.* (DUNE Collaboration), Reconstruction of interactions in the ProtoDUNE-SP detector with Pandora, Eur. Phys. J. C **83**, 618 (2023).
[25] A. Abed Abud *et al.*, Separation of track- and shower-like energy deposits in ProtoDUNE-SP using a convolutional neural network, Eur. Phys. J. C **82**, 903 (2022).
[26] R. Acciarri *et al.*, A study of electron recombination using highly ionizing particles in the ArgoNeuT liquid argon TPC, J. Instrum. **8**, P08005 (2013).
[27] S. Abbaslu *et al.* (DUNE Collaboration), Spatial and temporal evaluations of the liquid argon purity in ProtoDUNE-SP, J. Instrum. **20**, P09008 (2025).
[28] E. Gramellini *et al.* (LArIAT Collaboration), Measurement of the π^--Ar total hadronic cross section at the LArIAT experiment (2022).
[29] A. A. Abud *et al.* (DUNE Collaboration), First measurement of the total inelastic cross section of positively charged kaons on argon at energies between 5.0 and 7.5 GeV, Phys. Rev. D **110**, 092011 (2024).
[30] R. Barlow and C. Beeston, Fitting using finite Monte Carlo samples, Comput. Phys. Commun. **77**, 219 (1993).
[31] J. Conway, Incorporating nuisance parameters in likelihoods for multisource spectra, in *Presented at PHYSTAT 2011* (CERN, Geneva, Switzerland, 2011), pp. 115–120.
[32] J. Calcutt, C. Thorpe, K. Mahn, and L. Fields, Geant4Reweight: A framework for evaluating and propagating hadronic interaction uncertainties in Geant4, J. Instrum. **16**, P08042 (2021).
[33] S. Abbaslu *et al.*, First measurement of π^+-Ar and p-Ar total inelastic cross sections in the sub-GeV energy regime with ProtoDUNE-SP data, arXiv:2511.11925.
[34] DUNE Collaboration, Measurement of exclusive π^+-argon interactions using ProtoDUNE-SP, HEPData (collection), 10.17182/hepdata.169768 (2026).

S. Abbaslu,[114] A. Abed Abud,[35] R. Acciarri,[66] L. P. Accorsi,[193] M. A. Acero,[12] M. R. Adames,[193] G. Adamov,[72] M. Adamowski,[66] C. Adriano,[30] F. Akbar,[176] F. Alemanno,[98] N. S. Alex,[176] K. Allison,[43] M. Alrashed,[123] A. Alton,[13] R. Alvarez,[39] T. Alves,[89] A. Aman,[69] H. Amar,[84] P. Amedo,[85,84] J. Anderson,[8] D. A. Andrade,[88] C. Andreopoulos,[131] M. Andreotti,[95,67] M. P. Andrews,[66] F. Andrianala,[5] S. Andringa,[130] F. Anjarazafy,[5] S. Ansarifard,[114] D. Antic,[19] M. Antoniassi,[193] A. Aranda-Fernandez,[42] L. Arellano,[137] E. Arrieta Diaz,[181] M. A. Arroyave,[66] J. Asaadi,[197] M. Ascencio,[112] A. Ashkenazi,[194] D. Asner,[20] L. Asquith,[191] E. Atkin,[89] D. Auguste,[161] A. Aurisano,[40] V. Aushev,[127] D. Autiero,[113] D. Ávila Gómez,[58] M. B. Azam,[88] F. Azfar,[157] A. Back,[92] J. J. Back,[210] Y. Bae,[145] I. Bagaturia,[72] L. Bagby,[66] D. Baigarashev,[2] S. Balasubramanian,[66] A. Balboni,[67,95] P. Baldi,[24] W. Baldini,[95] J. Baldonedo,[207] B. Baller,[66] B. Bambah,[82] F. Barao,[130,116] D. Barbu,[21] G. Barenboim,[84] P. Barham Alzás,[35] G. J. Barker,[210] W. Barkhouse,[150] G. Barr,[157] A. Barros,[193] N. Barros,[130,61] D. Barrow,[157] J. L. Barrow,[145] A. Basharina-Freshville,[203] A. Bashyal,[20] V. Basque,[66] M. Bassani,[100] D. Basu,[151] C. Batchelor,[57] L. Bathe-Peters,[157] J. B. R. Battat,[211] F. Battisti,[93] J. Bautista,[145] F. Bay,[4] J. L. L. Bazo Alba,[170] J. F. Beacom,[155] E. Bechetoille,[113] B. Behera,[187] E. Belchior,[133] B. Bell,[54] G. Bell,[52] L. Bellantoni,[66] G. Bellettini,[104,168] V. Bellini,[94,31] O. Beltramello,[35] A. Belyaev,[216] C. Benitez Montiel,[84,10] D. Benjamin,[20] F. Bento Neves,[130] J. Berger,[44] S. Berkman,[141] J. Bermudez,[102] J. Bernal,[10] P. Bernardini,[98,180] A. Bersani,[97] E. Bertholet,[194] E. Bertolini,[99] S. Bertolucci,[93,17] M. Betancourt,[66] A. Betancur Rodríguez,[58] Y. Bezawada,[23] A. T. Bezerra,[62] A. Bhat,[37] V. Bhatnagar,[160] M. Bhattacharjee,[90] S. Bhattacharjee,[133] M. Bhattacharya,[66] S. Bhuller,[157] B. Bhuyan,[90] S. Biagi,[107] J. Bian,[24] K. Biery,[66] B. Bilki,[15,111] M. Bishai,[20] A. Blake,[128] F. D. Blaszczyk,[66] G. C. Blazey,[151] E. Blucher,[37] B. Bogart,[140] J. Boissevain,[132] S. Bolognesi,[34] T. Bolton,[123] L. Bomben,[99,110] M. Bonesini,[99,142] C. Bonilla-Diaz,[32] A. Booth,[173] F. Boran,[92] R. Borges Merlo,[30] N. Bostan,[111] G. Botogoske,[101] B. Bottino,[97,71] R. Bouet,[134] J. Boza,[44] J. Bracinik,[16] B. Brahma,[91] D. Brailsford,[128] F. Bramati,[99] A. Branca,[99] A. Brandt,[197] J. Bremer,[35] S. J. Brice,[66] V. Brio,[94] C. Brizzolari,[99,142] C. Bromberg,[141] J. Brooke,[19] A. Bross,[66] G. Brunetti,[99,142] M. B. Brunetti,[204] N. Buchanan,[44] H. Budd,[176] J. Buergi,[14] A. Bundock,[19] D. Burgardt,[212] S. Butchart,[191] G. Caceres V.,[23] R. Calabrese,[101] R. Calabrese,[95,67] J. Calcutt,[20,156] L. Calivers,[14] E. Calvo,[39] A. Caminata,[97] A. F. Camino,[169] W. Campanelli,[130] A. Campani,[97,71] A. Campos Benitez,[208] N. Canci,[101] J. Capó,[84] I. Caracas,[136] D. Caratelli,[27] D. Carber,[44] J. M. Carceller,[35] G. Carini,[20] B. Carlus,[113] M. F. Carneiro,[20] P. Carniti,[99,142] I. Caro Terrazas,[44] H. Carranza,[197] N. Carrara,[23] L. Carroll,[123] T. Carroll,[214] A. Carter,[177] E. Casarejos,[207] D. Casazza,[95] J. F. Castaño Forero,[7] F. A. Castaño,[6] C. Castromonte,[109] E. Catano-Mur,[213] C. Cattadori,[99] F. Cavalier,[161] F. Cavanna,[66] S. Centro,[159] G. Cerati,[66] C. Cerna,[115] A. Cervelli,[93] A. Cervera Villanueva,[84] J. Chakrani,[129] M. Chalifour,[35] A. Chappell,[210] A. Chatterjee,[167] B. Chauhan,[111] C. Chavez Barajas,[131] H. Chen,[20] M. Chen,[24] W. C. Chen,[199] Y. Chen,[185] Z. Chen,[24] D. Cherdack,[81] S. S. Chhibra,[173] C. Chi,[45] F. Chiapponi,[93] R. Chirco,[88] N. Chitirasreemadam,[104,168] K. Cho,[126] S. Choate,[111] G. Choi,[176] D. Chokheli,[72] P. S. Chong,[165] B. Chowdhury,[8]

D. Christian,[66] M. Chung,[202] E. Church,[158] M. F. Cicala,[203] M. Cicerchia,[159] V. Cicero,[93,17] R. Ciolini,[104] P. Clarke,[57] G. Cline,[129] A. G. Cocco,[101] J. A. B. Coelho,[162] A. Cohen,[162] J. Collazo,[207] J. Collot,[76] H. Combs,[208] J. M. Conrad,[138] L. Conti,[106] T. Contreras,[66] M. Convery,[185] K. Conway,[189] S. Copello,[103] P. Cova,[100,163] C. Cox,[177] L. Cremonesi,[173] J. I. Crespo-Anadón,[39] M. Crisler,[66] E. Cristaldo,[99,10] J. Crnkovic,[66] G. Crone,[203] R. Cross,[210] A. Cudd,[43] C. Cuesta,[39] Y. Cui,[26] F. Curciarello,[96] D. Cussans,[19] J. Dai,[76] O. Dalager,[66] W. Dallaway,[199] R. D'Amico,[95,67] H. da Motta,[33] Z. A. Dar,[213] R. Darby,[191] L. Da Silva Peres,[65] Q. David,[113] G. S. Davies,[146] S. Davini,[97] J. Dawson,[162] R. De Aguiar,[30] P. Debbins,[111] M. P. Decowski,[148,3] A. de Gouvêa,[152] P. C. De Holanda,[30] P. De Jong,[148,3] P. Del Amo Sanchez,[51] G. De Lauretis,[113] A. Delbart,[34] M. Delgado,[99,142] A. Dell'Acqua,[35] G. Delle Monache,[96] N. Delmonte,[100,163] P. De Lurgio,[8] G. De Matteis,[98,180] J. R. T. de Mello Neto,[65] A. P. A. de Mendonca,[30] D. M. DeMuth,[206] S. Dennis,[29] C. Densham,[179] P. Denton,[20] G. W. Deptuch,[20] A. De Roeck,[35] V. De Romeri,[84] J. P. Detje,[29] J. Devine,[35] K. Dhanmeher,[113] R. Dharmapalan,[79] M. Dias,[201] A. Diaz,[28] J. S. Díaz,[92] F. Díaz,[170] F. Di Capua,[101,147] A. Di Domenico,[182,105] S. Di Domizio,[97,71] S. Di Falco,[104] L. Di Giulio,[35] P. Ding,[66] L. Di Noto,[97,71] E. Diociaiuti,[96] G. Di Sciascio,[106] V. Di Silvestre,[182] C. Distefano,[107] R. Di Stefano,[106] R. Diurba,[14] M. Diwan,[20] Z. Djurcic,[8] S. Dolan,[35] M. Dolce,[212] M. J. Dolinski,[54] D. Domenici,[96] S. Dominguez,[39] S. Donati,[104,168] S. Doran,[112] D. Douglas,[185] T. A. Doyle,[189] F. Drielsma,[185] D. Duchesneau,[51] K. Duffy,[157] K. Dugas,[24] P. Dunne,[89] B. Dutta,[195] D. A. Dwyer,[129] A. S. Dyshkant,[151] S. Dytman,[169] M. Eads,[151] A. Earle,[191] S. Edayath,[112] D. Edmunds,[141] J. Eisch,[66] W. Emark,[151] P. Englezos,[178] A. Ereditato,[37] T. Erjavec,[23] C. O. Escobar,[66] J. J. Evans,[137] E. Ewart,[92] A. C. Ezeribe,[184] K. Fahey,[66] A. Falcone,[99,142] M. Fani',[145,132] D. Faragher,[145] C. Farnese,[102] Y. Farzan,[114] J. Felix,[77] Y. Feng,[112] M. Ferreira da Silva,[201] G. Ferry,[161] E. Fialova,[50] L. Fields,[153] P. Filip,[49] A. Filkins,[192] F. Filthaut,[148,174] G. Fiorillo,[101,147] M. Fiorini,[95,67] S. Fogarty,[44] W. Foreman,[132] J. Fowler,[55] J. Franc,[50] K. Francis,[151] D. Franco,[37] J. Franklin,[56] J. Freeman,[66] J. Fried,[20] A. Friedland,[185] M. Fucci,[189] S. Fuess,[66] I. K. Furic,[68] K. Furman,[173] A. P. Furmanski,[145] R. Gaba,[160] A. Gabrielli,[93,17] A. M. Gago,[170] F. Galizzi,[99,142] H. Gallagher,[200] M. Galli,[162] N. Gallice,[20] V. Galymov,[113] E. Gamberini,[35] T. Gamble,[184] R. Gandhi,[78] S. Ganguly,[66] F. Gao,[27] S. Gao,[20] D. Garcia-Gamez,[73] M. Á. García-Peris,[137] F. Gardim,[62] S. Gardiner,[66] A. Gartman,[50] A. Gauch,[14] P. Gauzzi,[182,105] S. Gazzana,[96] G. Ge,[45] N. Geffroy,[51] B. Gelli,[30] S. Gent,[188] L. Gerlach,[20] A. Ghosh,[112] T. Giammaria,[95,67] D. Gibin,[159,102] I. Gil-Botella,[39] A. Gioiosa,[106] S. Giovannella,[96] A. K. Giri,[91] V. Giusti,[104] D. Gnani,[129] O. Gogota,[127] S. Gollapinni,[132] K. Gollwitzer,[66] R. A. Gomes,[63] L. S. Gomez Fajardo,[183] D. Gonzalez-Diaz,[85] J. Gonzalez-Santome,[35] M. C. Goodman,[8] S. Goswami,[167] C. Gotti,[99] J. Goudeau,[133] C. Grace,[129] E. Gramellini,[137] R. Gran,[144] P. Granger,[35] C. Grant,[18] D. R. Gratieri,[70,30] G. Grauso,[101] P. Green,[157] S. Greenberg,[129,22] W. C. Griffith,[191] K. Grzelak,[209] L. Gu,[128] W. Gu,[20] V. Guarino,[8] M. Guarise,[95,67] R. Guenette,[137] M. Guerzoni,[93] D. Guffanti,[99,142] A. Guglielmi,[102] F. Y. Guo,[189] A. Gupta,[87] V. Gupta,[148,3] G. Gurung,[197] D. Gutierrez,[171] P. Guzowski,[137] M. M. Guzzo,[30] S. Gwon,[38] A. Habig,[144] L. Haegel,[113] R. Hafeji,[84,85] L. Hagaman,[37] A. Hahn,[66] J. Hakenmüller,[55] T. Hamernik,[66] P. Hamilton,[89] J. Hancock,[16] M. Handley,[29] F. Happacher,[96] B. Harris,[165] D. A. Harris,[217,66] L. Harris,[79] A. L. Hart,[173] J. Hartnell,[191] T. Hartnett,[179] J. Harton,[44] T. Hasegawa,[125] C. M. Hasnip,[35] R. Hatcher,[66] S. Hawkins,[141] J. Hays,[173] M. He,[81] A. Heavey,[66] K. M. Heeger,[215] A. Heindel,[189] J. Heise,[190] P. Hellmuth,[134] L. Henderson,[156] K. Herner,[66] V. Hewes,[40] A. Higuera,[175] A. Himmel,[66] E. Hinkle,[37] L. R. Hirsch,[193] J. Ho,[53] J. Hoefken Zink,[93] J. Hoff,[66] A. Holin,[179] T. Holvey,[157] C. Hong,[162] S. Horiuchi,[208] G. A. Horton-Smith,[123] R. Hosokawa,[118] T. Houdy,[161] B. Howard,[217,66] R. Howell,[176] I. Hristova,[179] M. S. Hronek,[66] H. Hua,[89] J. Huang,[23] R. G. Huang,[129] X. Huang,[146] Z. Hulcher,[185] A. Hussain,[123] G. Iles,[89] N. Ilic,[199] A. M. Iliescu,[96] R. Illingworth,[66] G. Ingratta,[217] A. Ioannisian,[216] M. Ismerio Oliveira,[65] C. M. Jackson,[158] V. Jain,[1] E. James,[66] W. Jang,[197] B. Jargowsky,[24] D. Jena,[66] I. Jentz,[214] C. Jiang,[119] J. Jiang,[189] A. Jipa,[21] J. H. Jo,[20] F. R. Joaquim,[130,116] W. Johnson,[187] C. Jollet,[134] R. Jones,[184] N. Jovancevic,[154] M. Judah,[169] C. K. Jung,[189] K. Y. Jung,[176] T. Junk,[66] Y. Jwa,[185,45] M. Kabirnezhad,[89] A. C. Kaboth,[177,179] I. Kadenko,[127] O. Kalikulov,[2] D. Kalra,[45] M. Kandemir,[60] S. Kar,[19] G. Karagiorgi,[45] G. Karaman,[111] A. Karcher,[129] Y. Karyotakis,[51] S. P. Kasetti,[133] L. Kashur,[44] A. Kauther,[151] N. Kazaryan,[216] L. Ke,[20] E. Kearns,[18] P. T. Keener,[165] K. J. Kelly,[195] R. Keloth,[208] E. Kemp,[30] O. Kemularia,[72] Y. Kermaidic,[161] W. Ketchum,[66] S. H. Kettell,[20] N. Khan,[89] A. Khvedelidze,[72] D. Kim,[195] J. Kim,[176] M. J. Kim,[66] S. Kim,[38] B. King,[66] M. King,[37] M. Kirby,[20] A. Kish,[66] J. Klein,[165] J. Kleykamp,[146] A. Klustova,[89] T. Kobilarcik,[66] L. Koch,[136] K. Koehler,[214] L. W. Koerner,[81] D. H. Koh,[185] M. Kordosky,[213] T. Kosc,[76] V. A. Kostelecký,[92] I. Kotler,[54] W. Krah,[148]

R. Kralik,[191] M. Kramer,[129] F. Krennrich,[112] T. Kroupova,[165] S. Kubota,[137] M. Kubu,[35] V. A. Kudryavtsev,[184] G. Kufatty,[69] S. Kuhlmann,[8] A. Kumar,[145] J. Kumar,[79] M. Kumar,[87] P. Kumar,[120] P. Kumar,[184] S. Kumaran,[24] J. Kunzmann,[14] V. Kus,[50] T. Kutter,[133] J. Kvasnicka,[49] T. Labree,[151] M. Lachat,[176] T. Lackey,[66] I. Lalău,[21] A. Lambert,[129] B. J. Land,[165] C. E. Lane,[54] N. Lane,[137] K. Lang,[198] T. Langford,[215] M. Langstaff,[137] F. Lanni,[35] J. Larkin,[176] P. Lasorak,[89] D. Last,[176] A. Laundrie,[214] G. Laurenti,[93] E. Lavaut,[161] H. Lay,[128] I. Lazanu,[21] R. LaZur,[44] M. Lazzaroni,[100,143] T. Le,[200] S. Leardini,[85] J. Learned,[79] T. LeCompte,[185] G. Lehmann Miotto,[35] R. Lehnert,[92] M. Leitner,[129] H. Lemoine,[144] D. Leon Silverio,[187] L. M. Lepin,[69] J.-Y. Li,[57] S. W. Li,[24] Y. Li,[20] R. Lima,[62] C. S. Lin,[129] D. Lindebaum,[19] S. Linden,[20] R. A. Lineros,[32] A. Lister,[214] B. R. Littlejohn,[88] J. Liu,[24] Y. Liu,[37] S. Lockwitz,[66] I. Lomidze,[72] K. Long,[89] J. Lopez,[6] I. López de Rego,[39] N. López-March,[84] J. M. LoSecco,[153] A. Lozano Sanchez,[54] X.-G. Lu,[210] K. B. Luk,[80,129,22] X. Luo,[27] E. Luppi,[95,67] A. A. Machado,[30] P. Machado,[66] C. T. Macias,[92] J. R. Macier,[66] M. MacMahon,[203] S. Magill,[8] C. Magueur,[161] K. Mahn,[141] A. Maio,[130,61] N. Majeed,[123] A. Major,[55] K. Majumdar,[131] A. Malige,[45] S. Mameli,[104] M. Man,[199] R. C. Mandujano,[24] J. Maneira,[130,61] S. Manly,[176] A. Mann,[200] K. Manolopoulos,[179] M. Manrique Plata,[92] S. Manthey Corchado,[39] L. Manzanillas-Velez,[51] E. Mao,[192] M. Marchan,[66] A. Marchionni,[66] D. Marfatia,[79] C. Mariani,[208] J. Maricic,[79] F. Marinho,[117] A. D. Marino,[43] T. Markiewicz,[185] F. Das Chagas Marques,[30] M. Marshak,[145] C. M. Marshall,[176] J. Marshall,[210] L. Martina,[98,180] J. Martín-Albo,[84] D. A. Martinez Caicedo,[187] M. Martinez-Casales,[66] F. Martínez López,[92] S. Martynenko,[20] V. Mascagna,[99] A. Mastbaum,[178] M. Masud,[38] F. Matichard,[129] G. Matteucci,[101,147] J. Matthews,[133] C. Mauger,[165] N. Mauri,[93,17] K. Mavrokoridis,[131] I. Mawby,[128] F. Mayhew,[141] T. McAskill,[211] N. McConkey,[173] B. McConnell,[92] K. S. McFarland,[176] C. McGivern,[66] C. McGrew,[189] A. McNab,[137] C. McNulty,[129] J. Mead,[148] L. Meazza,[99] V. C. N. Meddage,[68] A. Medhi,[90] M. Mehmood,[217] B. Mehta,[160] P. Mehta,[120] F. Mei,[93,17] P. Melas,[11] L. Mellet,[141] T. C. D. Melo,[62] O. Mena,[84] H. Mendez,[171] D. P. Méndez,[20] A. Menegolli,[103,164] G. Meng,[102] A. C. E. A. Mercuri,[193] A. Meregaglia,[134] M. D. Messier,[92] S. Metallo,[145] W. Metcalf,[133] M. Mewes,[92] H. Meyer,[212] T. Miao,[66] J. Micallef,[200,138] A. Miccoli,[98] G. Michna,[188] R. Milincic,[79] F. Miller,[214] G. Miller,[137] W. Miller,[145] A. Minotti,[99,142] L. Miralles Verge,[35] C. Mironov,[162] S. Miscetti,[96] C. S. Mishra,[66] P. Mishra,[82] S. R. Mishra,[186] D. Mladenov,[35] I. Mocioiu,[166] A. Mogan,[66] R. Mohanta,[82] T. A. Mohayai,[92] N. Mokhov,[66] J. Molina,[10] L. Molina Bueno,[84] E. Montagna,[93,17] A. Montanari,[93] C. Montanari,[103,66,164] D. Montanari,[66] D. Montanino,[98,180] L. M. Montaño Zetina,[41] M. Mooney,[44] A. F. Moor,[184] M. Moore,[185] Z. Moore,[192] D. Moreno,[7] G. Moreno-Granados,[208] O. Moreno-Palacios,[213] L. Morescalchi,[104] C. Morris,[81] E. Motuk,[203] C. A. Moura,[64] G. Mouster,[128] W. Mu,[66] L. Mualem,[28] J. Mueller,[66] M. Muether,[212] F. Muheim,[57] A. Muir,[52] Y. Mukhamejanov,[2] A. Mukhamejanova,[2] M. Mulhearn,[23] D. Munford,[81] L. J. Munteanu,[35] H. Muramatsu,[145] J. Muraz,[76] M. Murphy,[208] T. Murphy,[192] A. Mytilinaki,[179] J. Nachtman,[111] Y. Nagai,[59] S. Nagu,[135] D. Naples,[169] S. Narita,[118] J. Nava,[93,17] A. Navrer-Agasson,[89,137] N. Nayak,[20] M. Nebot-Guinot,[57] A. Nehm,[136] J. K. Nelson,[213] O. Neogi,[111] J. Nesbit,[214] M. Nessi,[66,35] D. Newbold,[179] M. Newcomer,[165] D. Newmark,[138] R. Nichol,[203] F. Nicolas-Arnaldos,[73] A. Nielsen,[24] A. Nikolica,[165] J. Nikolov,[154] E. Niner,[66] X. Ning,[20] K. Nishimura,[79] A. Norman,[66] A. Norrick,[66] F. Noto,[107] P. Novella,[84] A. Nowak,[128] J. A. Nowak,[128] M. Oberling,[8] J. P. Ochoa-Ricoux,[24] S. Oh,[55] S. B. Oh,[66] A. Olivier,[153] T. Olson,[81] Y. Onel,[111] Y. Onishchuk,[127] A. Oranday,[92] M. Osbiston,[210] J. A. Osorio Vélez,[6] L. O'Sullivan,[136] L. Otiniano Ormachea,[46,109] L. Pagani,[23] G. Palacio,[58] O. Palamara,[66] S. Palestini,[108] J. M. Paley,[66] M. Pallavicini,[97,71] C. Palomares,[39] S. Pan,[167] M. Panareo,[98,180] P. Panda,[82] V. Pandey,[66] W. Panduro Vazquez,[177] E. Pantic,[23] V. Paolone,[169] A. Papadopoulou,[132] R. Papaleo,[107] D. Papoulias,[11] S. Paramesvaran,[19] J. Park,[38] S. Parke,[66] S. Parsa,[14] S. Parveen,[120] M. Parvu,[21] D. Pasciuto,[104] S. Pascoli,[93,17] L. Pasqualini,[93,17] J. Pasternak,[89] G. Patel,[145] J. L. Paton,[66] C. Patrick,[57] L. Patrizii,[93] R. B. Patterson,[28] T. Patzak,[162] A. Paudel,[66] J. Paul,[148] L. Paulucci,[117] Z. Pavlovic,[66] G. Pawloski,[145] D. Payne,[131] A. Peake,[177] V. Pec,[49] E. Pedreschi,[104] S. J. M. Peeters,[191] W. Pellico,[66] E. Pennacchio,[113] A. Penzo,[111] O. L. G. Peres,[30] Y. F. Perez Gonzalez,[56] L. Pérez-Molina,[39] C. Pernas,[213] J. Perry,[57] D. Pershey,[69] G. Pessina,[99] G. Petrillo,[185] C. Petta,[94,31] R. Petti,[186] M. Pfaff,[89] V. Pia,[93,17] G. M. Piacentino,[106] L. Pickering,[179,177] L. Pierini,[67,95] F. Pietropaolo,[35,102] V. L. Pimentel,[47,30] G. Pinaroli,[20] S. Pincha,[90] J. Pinchault,[51] K. Pitts,[208] P. Plesniak,[89] K. Pletcher,[141] K. Plows,[157] C. Pollack,[171] T. Pollmann,[148,3] F. Pompa,[84] M. Artero Pons,[159] X. Pons,[35] N. Poonthottathil,[87,112] V. Popov,[194] F. Poppi,[93,17] J. Porter,[191] L. G. Porto Paixão,[30] M. Potekhin,[20] M. Pozzato,[93,17] R. Pradhan,[91] T. Prakash,[129] M. Prest,[99] F. Psihas,[66] D. Pugnere,[113] D. Pullia,[35,162] X. Qian,[20]

J. Queen,[55] J. L. Raaf,[66] M. Rabelhofer,[92] V. Radeka,[20] J. Rademacker,[19] F. Raffaelli,[104] A. Rafique,[8] A. Rahe,[151] S. Rajagopalan,[20] M. Rajaoalisoa,[40] I. Rakhno,[66] L. Rakotondravohitra,[5] M. A. Ralaikoto,[5] L. Ralte,[91] M. A. Ramirez Delgado,[165] B. Ramson,[66] S. S. Randriamanampisoa,[5] A. Rappoldi,[103,164] G. Raselli,[103,164] T. Rath,[187] P. Ratoff,[128] R. Ray,[66] H. Razafinime,[40] R. F. Razakamiandra,[189] E. M. Rea,[145] J. S. Real,[76] B. Rebel,[214,66] R. Rechenmacher,[66] J. Reichenbacher,[187] S. D. Reitzner,[66] E. Renner,[132] S. Repetto,[97,71] S. Rescia,[20] F. Resnati,[35] C. Reynolds,[173] M. Ribas,[193] S. Riboldi,[100] C. Riccio,[189] G. Riccobene,[107] J. S. Ricol,[76] M. Rigan,[191] A. Rikalo,[154] E. V. Rincón,[58] A. Ritchie-Yates,[177] D. Rivera,[132] A. Robert,[76] A. Roberts,[131] E. Robles,[24] M. Roda,[131] D. Rodas Rodríguez,[85] M. J. O. Rodrigues,[62] J. Rodriguez Rondon,[187] S. Rosauro-Alcaraz,[161] P. Rosier,[161] D. Ross,[141] M. Rossella,[103,164] M. Ross-Lonergan,[45] T. Rotsy,[5] N. Roy,[217] P. Roy,[212] P. Roy,[208] C. Rubbia,[74] D. Rudik,[101] A. Ruggeri,[93] G. Ruiz Ferreira,[137] K. Rushiya,[120] B. Russell,[138] S. Sacerdoti,[162] N. Saduyev,[2] S. K. Sahoo,[91] N. Sahu,[91] S. Sakhiyev,[2] P. Sala,[66] G. Salmoria,[193] S. Samanta,[97] M. C. Sanchez,[69] A. Sánchez-Castillo,[73] P. Sanchez-Lucas,[73] D. A. Sanders,[146] S. Sanfilippo,[107] D. Santoro,[100,163] N. Saoulidou,[11] P. Sapienza,[107] I. Sarcevic,[9] I. Sarra,[96] G. Savage,[66] V. Savinov,[169] G. Scanavini,[215] A. Scanu,[99] A. Scaramelli,[103] T. Schefke,[133] H. Schellman,[156,66] S. Schifano,[95,67] P. Schlabach,[66] D. Schmitz,[37] A. W. Schneider,[138] K. Scholberg,[55] A. Schroeder,[145] A. Schukraft,[66] B. Schuld,[43] S. Schwartz,[28] A. Segade,[207] E. Segreto,[30] A. Selyunin,[14] C. R. Senise,[201] J. Sensenig,[165] S. H. Seo,[66] D. Seppela,[141] M. H. Shaevitz,[45] P. Shanahan,[66] P. Sharma,[160] R. Kumar,[172] S. Sharma Poudel,[187] K. Shaw,[191] T. Shaw,[66] K. Shchablo,[113] J. Shen,[165] C. Shepherd-Themistocleous,[179] J. Shi,[29] W. Shi,[189] S. Shin,[121] S. Shivakoti,[212] A. Shmakov,[24] I. Shoemaker,[208] D. Shooltz,[141] R. Shrock,[189] M. Siden,[44] J. Silber,[129] L. Simard,[161] J. Sinclair,[185] G. Sinev,[187] Jaydip Singh,[23] J. Singh,[135] L. Singh,[48] P. Singh,[173] V. Singh,[48] S. Singh Chauhan,[160] R. Sipos,[35] C. Sironneau,[162] G. Sirri,[93] K. Siyeon,[38] K. Skarpaas,[185] J. Smedley,[176] J. Smith,[189] P. Smith,[92] J. Smolik,[50,49] M. Smy,[24] M. Snape,[210] E. L. Snider,[66] P. Snopok,[88] M. Soares Nunes,[66] H. Sobel,[24] M. Soderberg,[192] H. Sogarwal,[112] C. J. Solano Salinas,[205] S. Söldner-Rembold,[89] N. Solomey,[212] V. Solovov,[130] W. E. Sondheim,[132] M. Sorbara,[106] M. Sorel,[84] J. Soto-Oton,[84] A. Sousa,[40] K. Soustruznik,[36] D. Souza Correia,[33] F. Spinella,[104] J. Spitz,[140] N. J. C. Spooner,[184] D. Stalder,[10] M. Stancari,[66] L. Stanco,[159,102] J. Steenis,[23] R. Stein,[19] H. M. Steiner,[129] A. F. Steklain Lisbôa,[193] J. Stewart,[20] B. Stillwell,[37] J. Stock,[187] T. Stokes,[215] T. Strauss,[66] L. Strigari,[195] A. Stuart,[42] J. G. Suarez,[58] J. Subash,[16] A. Surdo,[98] L. Suter,[66] A. Sutton,[69] K. Sutton,[28] Y. Suvorov,[101,147] R. Svoboda,[23] S. K. Swain,[149] C. Sweeney,[112] B. Szczerbinska,[196] A. M. Szelc,[57] A. Sztuc,[203] A. Taffara,[104] N. Talukdar,[186] J. Tamara,[7] H. A. Tanaka,[185] S. Tang,[20] N. Taniuchi,[29] A. M. Tapia Casanova,[139] A. Tapper,[89] S. Tariq,[66] E. Tatar,[83] R. Tayloe,[92] A. M. Teklu,[189] K. Tellez Giron Flores,[20] J. Tena Vidal,[194] P. Tennessen,[129,4] M. Tenti,[93] K. Terao,[185] F. Terranova,[99,142] G. Testera,[97] T. Thakore,[40] A. Thea,[179] S. Thomas,[192] A. Thompson,[152] C. Thorpe,[137] S. C. Timm,[66] E. Tiras,[60,111] V. Tishchenko,[20] S. Tiwari,[176] N. Todorović,[154] L. Tomassetti,[95,67] A. Tonazzo,[162] D. Torbunov,[20] D. Torres Muñoz,[187] M. Torti,[99,142] M. Tortola,[84] Y. Torun,[88] N. Tosi,[93] D. Totani,[44] M. Toups,[66] C. Touramanis,[131] V. Trabattoni,[100] D. Tran,[81] J. Trevor,[28] E. Triller,[141] S. Trilov,[19] D. Trotta,[99] J. Truchon,[214] D. Truncali,[182,105] W. H. Trzaska,[122] Y. Tsai,[24] Y.-T. Tsai,[185] Z. Tsamalaidze,[72] K. V. Tsang,[185] N. Tsverava,[72] S. Z. Tu,[119] S. Tufanli,[35] C. Tunnell,[175] J. Turner,[56] M. Tuzi,[84] M. Tzanov,[133] M. A. Uchida,[29] J. Ureña González,[84] J. Urheim,[92] T. Usher,[185] H. Utaegbulam,[176] S. Uzunyan,[151] M. R. Vagins,[124,24] P. Vahle,[213] G. A. Valdiviesso,[62] E. Valencia,[77] R. Valentim,[201] Z. Vallari,[155] E. Vallazza,[99] J. W. F. Valle,[84] R. Van Berg,[165] D. V. Forero,[139] A. Vannozzi,[96] M. Van Nuland-Troost,[148] F. Varanini,[102] D. Vargas Oliva,[199] N. Vaughan,[156] K. Vaziri,[66] A. Vázquez-Ramos,[73] J. Vega,[46] J. Vences,[130,61] S. Ventura,[102] A. Verdugo,[39] M. Verzocchi,[66] K. Vetter,[66] M. Vicenzi,[20] H. Vieira de Souza,[162] C. Vignoli,[75] C. Vilela,[130] E. Villa,[35] S. Viola,[107] B. Viren,[20] G. V. Stenico,[57] R. Vizarreta,[176] A. P. Vizcaya Hernandez,[44] S. Vlachos,[137] G. Vorobyev,[186] Q. Vuong,[176] A. V. Waldron,[173] L. Walker,[81] H. Wallace,[177] M. Wallach,[141] J. Walsh,[141] T. Walton,[66] L. Wan,[66] B. Wang,[111] H. Wang,[25] J. Wang,[187] M. H. L. S. Wang,[66] X. Wang,[66] Y. Wang,[86] D. Warner,[44] L. Warsame,[179] M. O. Wascko,[157,179] D. Waters,[203] A. Watson,[16] K. Wawrowska,[179,191] A. Weber,[136,66] C. M. Weber,[145] M. Weber,[14] H. Wei,[133] A. Weinstein,[112] S. Westerdale,[26] M. Wetstein,[112] K. Whalen,[179] A. J. White,[215] L. H. Whitehead,[29] D. Whittington,[192] F. Wieler,[193] J. Wilhlemi,[215] M. J. Wilking,[145] A. Wilkinson,[210] C. Wilkinson,[129] F. Wilson,[179] R. J. Wilson,[44] P. Winter,[8] J. Wolcott,[200] J. Wolfs,[176] T. Wongjirad,[200] A. Wood,[81] K. Wood,[129] E. Worcester,[20] M. Worcester,[20] K. Wresilo,[29] M. Wright,[137] M. Wrobel,[44] S. Wu,[145] W. Wu,[24] Z. Wu,[24] M. Wurm,[136] J. Wyenberg,[53] B. M. Wynne,[57] Y. Xiao,[24] I. Xiotidis,[89] B. Yaeggy,[40] N. Yahlali,[84] E. Yandel,[27]

G. Yang,[20,189] J. Yang,[80] T. Yang,[66] A. Yankelevich,[24] L. Yates,[66] U. Yevarouskaya,[189] K. Yonehara,[66] T. Young,[150] B. Yu,[20] H. Yu,[20] J. Yu,[197] W. Yuan,[57] M. Zabloudil,[50] R. Zaki,[217] J. Zalesak,[49] L. Zambelli,[51] B. Zamorano,[73] A. Zani,[100] O. Zapata,[6] L. Zazueta,[192] G. P. Zeller,[66] J. Zennamo,[66] J. Zettlemoyer,[66] K. Zeug,[214] C. Zhang,[20] S. Zhang,[92] Y. Zhang,[20] L. Zhao,[24] M. Zhao,[20] E. D. Zimmerman,[43] S. Zucchelli,[93,17] V. Zutshi,[151] and R. Zwaska[66]

(DUNE Collaboration)

[1]*University of Albany, SUNY, Albany, New York 12222, USA*
[2]*Institute of Nuclear Physics at Almaty, Almaty 050032, Kazakhstan*
[3]*University of Amsterdam, NL-1098 XG Amsterdam, The Netherlands*
[4]*Antalya Bilim University, 07190, Döşemealtı/Antalya, Turkey*
[5]*University of Antananarivo, Antananarivo 101, Madagascar*
[6]*University of Antioquia, Medellín, Colombia*
[7]*Universidad Antonio Nariño, Bogotá, Colombia*
[8]*Argonne National Laboratory, Argonne, Illinois 60439, USA*
[9]*University of Arizona, Tucson, Arizona 85721, USA*
[10]*Universidad Nacional de Asunción, San Lorenzo, Paraguay*
[11]*University of Athens, Zografou GR 157 84, Greece*
[12]*Universidad del Atlántico, Barranquilla, Atlántico, Colombia*
[13]*Augustana University, Sioux Falls, South Dakota 57197, USA*
[14]*University of Bern, CH-3012 Bern, Switzerland*
[15]*Beykent University, Istanbul, Turkey*
[16]*University of Birmingham, Birmingham B15 2TT, United Kingdom*
[17]*Università di Bologna, 40127 Bologna, Italy*
[18]*Boston University, Boston, Massachusetts 02215, USA*
[19]*University of Bristol, Bristol BS8 1TL, United Kingdom*
[20]*Brookhaven National Laboratory, Upton, New York 11973, USA*
[21]*University of Bucharest, Bucharest, Romania*
[22]*University of California Berkeley, Berkeley, California 94720, USA*
[23]*University of California Davis, Davis, California 95616, USA*
[24]*University of California Irvine, Irvine, California 92697, USA*
[25]*University of California Los Angeles, Los Angeles, California 90095, USA*
[26]*University of California Riverside, Riverside California 92521, USA*
[27]*University of California Santa Barbara, Santa Barbara, California 93106, USA*
[28]*California Institute of Technology, Pasadena, California 91125, USA*
[29]*University of Cambridge, Cambridge CB3 0HE, United Kingdom*
[30]*Universidade Estadual de Campinas, Campinas—São Paulo, 13083-970, Brazil*
[31]*Università di Catania, 2–95131 Catania, Italy*
[32]*Universidad Católica del Norte, Antofagasta, Chile*
[33]*Centro Brasileiro de Pesquisas Físicas, Rio de Janeiro, Rio de Janeiro 22290-180, Brazil*
[34]*IRFU, CEA, Université Paris-Saclay, F-91191 Gif-sur-Yvette, France*
[35]*CERN, The European Organization for Nuclear Research, 1211 Meyrin, Switzerland*
[36]*Institute of Particle and Nuclear Physics of the Faculty of Mathematics and Physics of the Charles University, 180 00 Prague 8, Czech Republic*
[37]*University of Chicago, Chicago, Illinois 60637, USA*
[38]*Chung-Ang University, Seoul 06974, South Korea*
[39]*CIEMAT, Centro de Investigaciones Energéticas, Medioambientales y Tecnológicas, E-28040 Madrid, Spain*
[40]*University of Cincinnati, Cincinnati, Ohio 45221, USA*
[41]*Centro de Investigación y de Estudios Avanzados del Instituto Politécnico Nacional (Cinvestav), Mexico City, Mexico*
[42]*Universidad de Colima, Colima, Mexico*
[43]*University of Colorado Boulder, Boulder, Colorado 80309, USA*
[44]*Colorado State University, Fort Collins, Colorado 80523, USA*
[45]*Columbia University, New York, New York 10027, USA*
[46]*Comisión Nacional de Investigación y Desarrollo Aeroespacial, Lima, Peru*

[47]*Centro de Tecnologia da Informacao Renato Archer, Amarais—Campinas, São Paulo—CEP 13069-901, Brazil*
[48]*Central University of South Bihar, Gaya, 824236, India*
[49]*Institute of Physics, Czech Academy of Sciences, 182 00 Prague 8, Czech Republic*
[50]*Czech Technical University, 115 19 Prague 1, Czech Republic*
[51]*Laboratoire d'Annecy de Physique des Particules, Université Savoie Mont Blanc, CNRS, LAPP-IN2P3, 74000 Annecy, France*
[52]*Daresbury Laboratory, Cheshire WA4 4AD, United Kingdom*
[53]*Dordt University, Sioux Center, Iowa 51250, USA*
[54]*Drexel University, Philadelphia, Pennsylvania 19104, USA*
[55]*Duke University, Durham, North Carolina 27708, USA*
[56]*Durham University, Durham DH1 3LE, United Kingdom*
[57]*University of Edinburgh, Edinburgh EH8 9YL, United Kingdom*
[58]*Universidad EIA, Envigado, Antioquia, Colombia*
[59]*Eötvös Loránd University, 1053 Budapest, Hungary*
[60]*Erciyes University, Kayseri, Turkey*
[61]*Faculdade de Ciências da Universidade de Lisboa—FCUL, 1749-016 Lisboa, Portugal*
[62]*Universidade Federal de Alfenas, Poços de Caldas—Minas Gerais, 37715-400, Brazil*
[63]*Universidade Federal de Goias, Goiania, Goiás 74690-900, Brazil*
[64]*Universidade Federal do ABC, Santo André—São Paulo, 09210-580, Brazil*
[65]*Universidade Federal do Rio de Janeiro, Rio de Janeiro—Rio de Janeiro, 21941-901, Brazil*
[66]*Fermi National Accelerator Laboratory, Batavia, Illinois 60510, USA*
[67]*University of Ferrara, Ferrara, Italy*
[68]*University of Florida, Gainesville, Florida 32611-8440, USA*
[69]*Florida State University, Tallahassee, Florida 32306, USA*
[70]*Fluminense Federal University, 9 Icaraí Niterói—Rio de Janeiro, 24220-900, Brazil*
[71]*Università degli Studi di Genova, Genova, Italy*
[72]*Georgian Technical University, Tbilisi, Georgia*
[73]*University of Granada and CAFPE, 18002 Granada, Spain*
[74]*Gran Sasso Science Institute, L'Aquila, Italy*
[75]*Laboratori Nazionali del Gran Sasso, L'Aquila AQ, Italy*
[76]*University Grenoble Alpes, CNRS, Grenoble INP, LPSC-IN2P3, 38000 Grenoble, France*
[77]*Universidad de Guanajuato, Guanajuato, C.P. 37000, Mexico*
[78]*Harish-Chandra Research Institute, Jhunsi, Allahabad 211 019, India*
[79]*University of Hawaii, Honolulu, Hawaii 96822, USA*
[80]*Hong Kong University of Science and Technology, Kowloon, Hong Kong, China*
[81]*University of Houston, Houston, Texas 77204, USA*
[82]*University of Hyderabad, Gachibowli, Hyderabad—500 046, India*
[83]*Idaho State University, Pocatello, Idaho 83209, USA*
[84]*Instituto de Física Corpuscular, CSIC and Universitat de València, 46980 Paterna, Valencia, Spain*
[85]*Instituto Galego de Física de Altas Enerxías, University of Santiago de Compostela, Santiago de Compostela, 15782, Spain*
[86]*Institute of High Energy Physics, Chinese Academy of Sciences, Beijing, China*
[87]*Indian Institute of Technology Kanpur, Uttar Pradesh 208016, India*
[88]*Illinois Institute of Technology, Chicago, Illinois 60616, USA*
[89]*Imperial College of Science, Technology and Medicine, London SW7 2BZ, United Kingdom*
[90]*Indian Institute of Technology Guwahati, Guwahati, 781 039, India*
[91]*Indian Institute of Technology Hyderabad, Hyderabad, 502285, India*
[92]*Indiana University, Bloomington, Indiana 47405, USA*
[93]*Istituto Nazionale di Fisica Nucleare Sezione di Bologna, 40127 Bologna BO, Italy*
[94]*Istituto Nazionale di Fisica Nucleare Sezione di Catania, I-95123 Catania, Italy*
[95]*Istituto Nazionale di Fisica Nucleare Sezione di Ferrara, I-44122 Ferrara, Italy*
[96]*Istituto Nazionale di Fisica Nucleare Laboratori Nazionali di Frascati, Frascati, Roma, Italy*
[97]*Istituto Nazionale di Fisica Nucleare Sezione di Genova, 16146 Genova GE, Italy*
[98]*Istituto Nazionale di Fisica Nucleare Sezione di Lecce, 73100—Lecce, Italy*
[99]*Istituto Nazionale di Fisica Nucleare Sezione di Milano Bicocca, 3—I-20126 Milano, Italy*
[100]*Istituto Nazionale di Fisica Nucleare Sezione di Milano, 20133 Milano, Italy*
[101]*Istituto Nazionale di Fisica Nucleare Sezione di Napoli, I-80126 Napoli, Italy*
[102]*Istituto Nazionale di Fisica Nucleare Sezione di Padova, 35131 Padova, Italy*
[103]*Istituto Nazionale di Fisica Nucleare Sezione di Pavia, I-27100 Pavia, Italy*

[104]*Istituto Nazionale di Fisica Nucleare Laboratori Nazionali di Pisa, Pisa PI, Italy*
[105]*Istituto Nazionale di Fisica Nucleare Sezione di Roma, 00185 Roma RM, Italy*
[106]*Istituto Nazionale di Fisica Nucleare Roma Tor Vergata, 00133 Roma RM, Italy*
[107]*Istituto Nazionale di Fisica Nucleare Laboratori Nazionali del Sud, 95123 Catania, Italy*
[108]*Istituto Nazionale di Fisica Nucleare, Sezione di Torino, Turin, Italy*
[109]*Universidad Nacional de Ingeniería, Lima 25, Peru*
[110]*University of Insubria, Via Ravasi, 2, 21100 Varese VA, Italy*
[111]*University of Iowa, Iowa City, Iowa 52242, USA*
[112]*Iowa State University, Ames, Iowa 50011, USA*
[113]*Institut de Physique des 2 Infinis de Lyon, 69622 Villeurbanne, France*
[114]*Institute for Research in Fundamental Sciences, Tehran, Iran*
[115]*Particle Physics and Cosmology International Research Laboratory, Chicago, Illinois 60637, USA*
[116]*Instituto Superior Técnico—IST, Universidade de Lisboa, 1049-001 Lisboa, Portugal*
[117]*Instituto Tecnológico de Aeronáutica, Sao Jose dos Campos, Brazil*
[118]*Iwate University, Morioka, Iwate 020-8551, Japan*
[119]*Jackson State University, Jackson, Mississippi 39217, USA*
[120]*Jawaharlal Nehru University, New Delhi 110067, India*
[121]*Jeonbuk National University, Jeonrabuk-do 54896, South Korea*
[122]*Jyväskylä University, FI-40014 Jyväskylä, Finland*
[123]*Kansas State University, Manhattan, Kansas 66506, USA*
[124]*Kavli Institute for the Physics and Mathematics of the Universe, Kashiwa, Chiba 277-8583, Japan*
[125]*High Energy Accelerator Research Organization (KEK), Ibaraki, 305-0801, Japan*
[126]*Korea Institute of Science and Technology Information, Daejeon, 34141, South Korea*
[127]*Taras Shevchenko National University of Kyiv, 01601 Kyiv, Ukraine*
[128]*Lancaster University, Lancaster LA1 4YB, United Kingdom*
[129]*Lawrence Berkeley National Laboratory, Berkeley, California 94720, USA*
[130]*Laboratório de Instrumentação e Física Experimental de Partículas, 1649-003 Lisboa and 3004-516 Coimbra, Portugal*
[131]*University of Liverpool, L69 7ZE, Liverpool, United Kingdom*
[132]*Los Alamos National Laboratory, Los Alamos, New Mexico 87545, USA*
[133]*Louisiana State University, Baton Rouge, Louisiana 70803, USA*
[134]*Laboratoire de Physique des Deux Infinis Bordeaux—IN2P3, F-33175 Gradignan, Bordeaux, France*
[135]*University of Lucknow, Uttar Pradesh 226007, India*
[136]*Johannes Gutenberg-Universität Mainz, 55122 Mainz, Germany*
[137]*University of Manchester, Manchester M13 9PL, United Kingdom*
[138]*Massachusetts Institute of Technology, Cambridge, Massachusetts 02139, USA*
[139]*University of Medellín, Medellín, 050026 Colombia*
[140]*University of Michigan, Ann Arbor, Michigan 48109, USA*
[141]*Michigan State University, East Lansing, Michigan 48824, USA*
[142]*Università di Milano Bicocca, 20126 Milano, Italy*
[143]*Università degli Studi di Milano, I-20133 Milano, Italy*
[144]*University of Minnesota Duluth, Duluth, Minnesota 55812, USA*
[145]*University of Minnesota Twin Cities, Minneapolis, Minnesota 55455, USA*
[146]*University of Mississippi, University, Mississippi 38677, USA*
[147]*Università degli Studi di Napoli Federico II, 80138 Napoli NA, Italy*
[148]*Nikhef National Institute of Subatomic Physics, 1098 XG Amsterdam, Netherlands*
[149]*National Institute of Science Education and Research (NISER), Odisha 752050, India*
[150]*University of North Dakota, Grand Forks, North Dakota 58202-8357, USA*
[151]*Northern Illinois University, DeKalb, Illinois 60115, USA*
[152]*Northwestern University, Evanston, Illinois 60208, USA*
[153]*University of Notre Dame, Notre Dame, Indiana 46556, USA*
[154]*University of Novi Sad, 21102 Novi Sad, Serbia*
[155]*Ohio State University, Columbus, Ohio 43210, USA*
[156]*Oregon State University, Corvallis, Oregon 97331, USA*
[157]*University of Oxford, Oxford, OX1 3RH, United Kingdom*
[158]*Pacific Northwest National Laboratory, Richland, Washington 99352, USA*
[159]*Universtà degli Studi di Padova, I-35131 Padova, Italy*
[160]*Panjab University, Chandigarh, 160014, India*
[161]*Université Paris-Saclay, CNRS/IN2P3, IJCLab, 91405 Orsay, France*
[162]*Université Paris Cité, CNRS, Astroparticule et Cosmologie, Paris, France*

[163]*University of Parma, 43121 Parma PR, Italy*
[164]*Università degli Studi di Pavia, 27100 Pavia PV, Italy*
[165]*University of Pennsylvania, Philadelphia, Pennsylvania 19104, USA*
[166]*Pennsylvania State University, University Park, Pennsylvania 16802, USA*
[167]*Physical Research Laboratory, Ahmedabad 380 009, India*
[168]*Università di Pisa, I-56127 Pisa, Italy*
[169]*University of Pittsburgh, Pittsburgh, Pennsylvania 15260, USA*
[170]*Pontificia Universidad Católica del Perú, Lima, Peru*
[171]*University of Puerto Rico, Mayaguez 00681, Puerto Rico, USA*
[172]*Punjab Agricultural University, Ludhiana 141004, India*
[173]*Queen Mary University of London, London E1 4NS, United Kingdom*
[174]*Radboud University, NL-6525 AJ Nijmegen, Netherlands*
[175]*Rice University, Houston, Texas 77005, USA*
[176]*University of Rochester, Rochester, New York 14627, USA*
[177]*Royal Holloway College London, London, TW20 0EX, United Kingdom*
[178]*Rutgers University, Piscataway, New Jersey 08854, USA*
[179]*STFC Rutherford Appleton Laboratory, Didcot OX11 0QX, United Kingdom*
[180]*Università del Salento, 73100 Lecce, Italy*
[181]*Universidad del Magdalena, Santa Marta, Colombia*
[182]*Sapienza University of Rome, 00185 Roma RM, Italy*
[183]*Universidad Sergio Arboleda, 11022 Bogotá, Colombia*
[184]*University of Sheffield, Sheffield S3 7RH, United Kingdom*
[185]*SLAC National Accelerator Laboratory, Menlo Park, California 94025, USA*
[186]*University of South Carolina, Columbia, South Carolina 29208, USA*
[187]*South Dakota School of Mines and Technology, Rapid City, South Dakota 57701, USA*
[188]*South Dakota State University, Brookings, South Dakota 57007, USA*
[189]*Stony Brook University, SUNY, Stony Brook, New York 11794, USA*
[190]*Sanford Underground Research Facility, Lead, South Dakota 57754, USA*
[191]*University of Sussex, Brighton, BN1 9RH, United Kingdom*
[192]*Syracuse University, Syracuse, New York 13244, USA*
[193]*Universidade Tecnológica Federal do Paraná, Curitiba, Brazil*
[194]*Tel Aviv University, Tel Aviv-Yafo, Israel*
[195]*Texas A&M University, College Station, Texas 77840, USA*
[196]*Texas A&M University–Corpus Christi, Corpus Christi, Texas 78412, USA*
[197]*University of Texas at Arlington, Arlington, Texas 76019, USA*
[198]*University of Texas at Austin, Austin, Texas 78712, USA*
[199]*University of Toronto, Toronto, Ontario M5S 1A1, Canada*
[200]*Tufts University, Medford, Massachusetts 02155, USA*
[201]*Universidade Federal de São Paulo, 09913-030, São Paulo, Brazil*
[202]*Ulsan National Institute of Science and Technology, Ulsan 689-798, South Korea*
[203]*University College London, London, WC1E 6BT, United Kingdom*
[204]*University of Kansas, Lawrence, Kansas 66045, USA*
[205]*Universidad Nacional Mayor de San Marcos, Lima, Peru*
[206]*Valley City State University, Valley City, North Dakota 58072, USA*
[207]*University of Vigo, E-36310 Vigo, Spain*
[208]*Virginia Tech, Blacksburg, Virginia 24060, USA*
[209]*University of Warsaw, 02-093 Warsaw, Poland*
[210]*University of Warwick, Coventry CV4 7AL, United Kingdom*
[211]*Wellesley College, Wellesley, Massachusetts 02481, USA*
[212]*Wichita State University, Wichita, Kansas 67260, USA*
[213]*William and Mary, Williamsburg, Virginia 23187, USA*
[214]*University of Wisconsin Madison, Madison, Wisconsin 53706, USA*
[215]*Yale University, New Haven, Connecticut 06520, USA*
[216]*Yerevan Institute for Theoretical Physics and Modeling, Yerevan 0036, Armenia*
[217]*York University, Toronto, Ontario M3J 1P3, Canada*